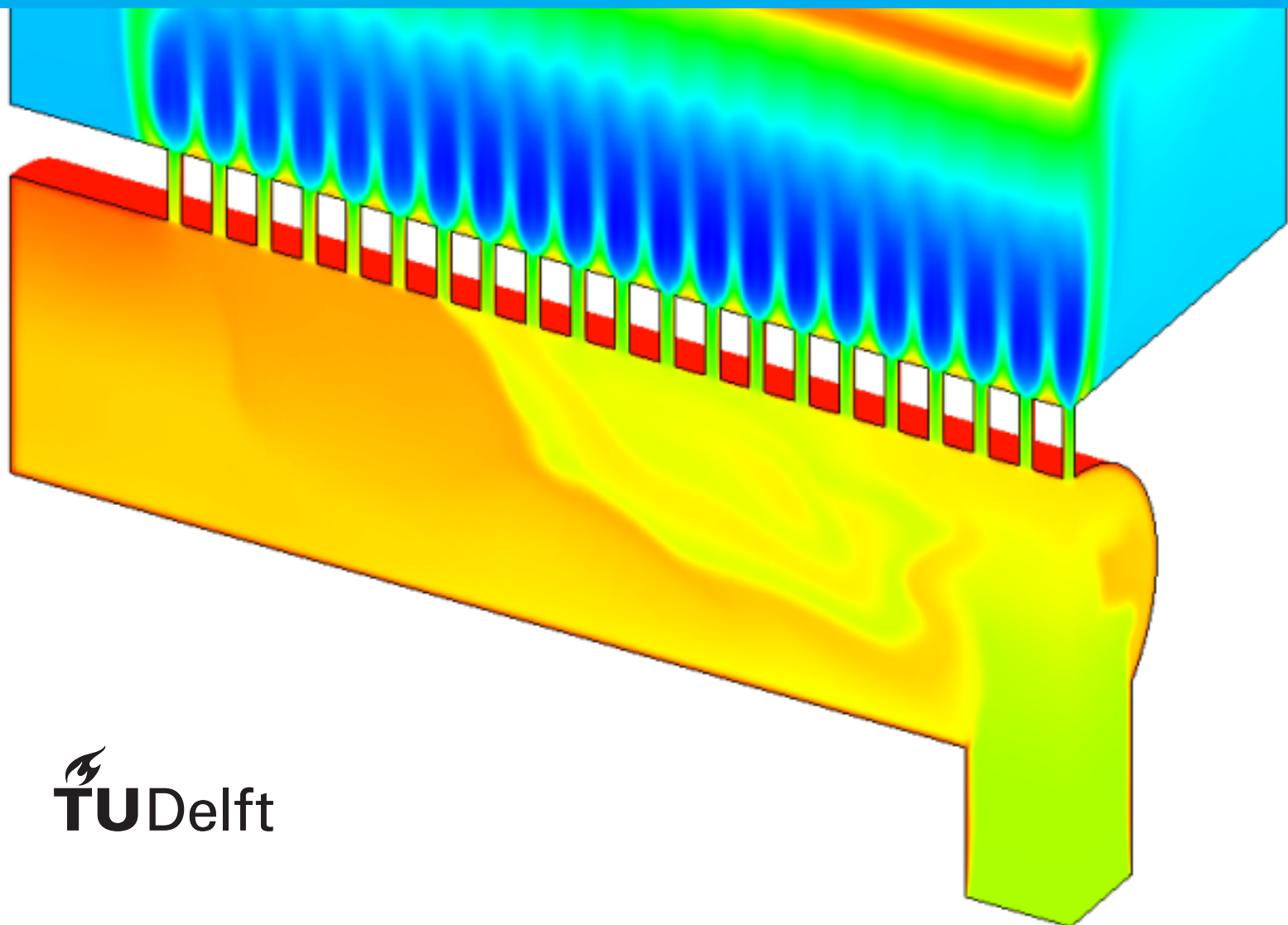# Flow Analysis of a Physical Vapour Deposition Process in OpenFOAM

Chibuikem S. Obiji

Flow Analysis of a Physical Vapour Deposition Process in OpenFOAM

by

Chibuikem S. Obiji

to obtain the degree of Master of Science
at the Delft University of Technology,
to be defended publicly on Friday August 30, 2019 at 10:30 AM.

This thesis is confidential and cannot be made public until August 20, 2021.

An electronic version of this thesis is available at http://repository.tudelft.nl/.

TU Delft

Abstract

Tata Steel employs physical vapour deposition (PVD) as a novel galvanization technique in their line production to prevent corrosion. In this process, zinc is evaporated in a vapour distribution box (VDB) and directed via nozzles into a vacuum where it is deposited on a steel substrate. In order to reduce stray deposition, achieve high and uniform mass flow rate from the nozzles and avoid condensation, understanding of the flow phenomena in the VDB and nozzles are necessary. Seeing that the PVD process is carried out at high temperatures in vacuum which makes it infeasible to experimentally characterise the flow for optimization purposes, thus, this research utilizes computational fluid dynamics (CFD).

In this study, the flow behaviour of the zinc vapour in the VDB and nozzles are investigated by solving the fluid governing equations numerically using finite volume method (FVM) in openFOAM. This analysis is done using the pressure-based sonicFoam solver to cope with the subsonic flow in the VDB and supersonic flow in the nozzles. The mass flow rate was compared to the ideal isentropic expression and experimental results. Regions in the set-up with high probability of condensation was investigated using a four coefficient Antoine equation.

A uniform pressure build-up in the VDB enabled uniform deposition. Around the corner of the inlet channel, a stable recirculation pattern affected the nozzle flow, however, this effect reduced as the outlet pressure decreased. The simulated total mass flow rate was greater than the experimental data by a factor of four possibly as a result of numerical errors and experimental stray depositions. And the simulated nozzle mass flow rate was less than the analytical isentropic expression by a factor of five due to the nozzle viscous boundary effect, and VDB wall heating. The mass flow rate from the nozzles decreased with increase in distance from the inlet channel. However, the nozzles far away are less likely to form zinc droplets as compared to those close to the inlet stream. For scale-up under the same conditions, it is expected that non-uniformity would be pronounced and the effect of the small eddies would become more significant. Thus, the simulation of the PVD process gives a qualitative description of the flow and a first approximation for the mass flow rate. To further improve the mass flow prediction, the sensitivity of the mass flow rate depending on the melt temperature and inlet velocity boundary condition should be studied in future works.

Contents

List of Figures

List of Tables

Nomenclature

Acronyms

bf   Back Flow

CFD   Computational Fluid Dynamics

FOAM   Field Operation and Manipulation

FVM   Finite Volume Method

HDG   Hot Deep Galvanizing

PISO   Pressure Implicit with Splitting of Operator

PVD   Physical Vapour Deposition

SIMPLE   Semi-Implicit Method for Pressure-Linked Equations

VDB   Vapour Distribution Box

Dimensionless Numbers

Kn   Knudsen Number

M   Mach Number

Pr   Prandtl Number

Re   Reynolds Number

Greek Symbols

γ Specific Heat Ratio

$\mathscr{O}$ Order of Magnitude

μ Dynamic Viscosity

∇ Nabla

∂ Partial Change of Variable

ψ Compressibility

ρ Density

$\sum$ Summation

Roman Symbols

$\dot{m}$	Mass Flow Rate	kg/s
$\hat{u}$	Specific Internal Energy	J/kg
A, B, C, D	Antoine Coefficients	-
g	Gravitational Acceleration	m/s^2
I	Turbulence Intensity	-
q	Heat Flux	W/m^2
A	Cross-sectional Area of Nozzle	m^2
a	Speed of Sound	m/s
a_N^v	Off-diagonal Matrix Coefficient	-
a_P^v	Diagonal Matrix Coefficient	-
A_s, T_s	Sutherland Coefficients	$Pa\,s\,K^{0.5}$, K
c_p	Specific Heat Capacity at Constant Pressure	J/kg/K
c_v	Specific Heat Capacity at Constant Volume	J/kg/K
d	Nozzle Diameter	m
d	Total Change of Variable	-
e	Total Energy	J/Kg
h	Specific Enthalpy	J/kg
L	Length Scale	m
l	Molecular Mean Free Path	m
P	Pressure	Pa
R	Gas Constant	J/K/mol
T	Temperature	K
t	Time	s
U	Flow Speed	m/s
v	Flow Velocity	m/s
x, y, z	Rectangular Coordinates	m

Sub- and Superscripts

$'$	Fluctuation
$^-$	Mean
$_{rms}$	Root Mean Square
$_*$	Critical
$_o$	Stagnation
$_s$	Isentropic
$_t$	Total

1

Introduction

1.1. Motivation

Corrosion is a natural phenomena which can be detrimental and cost huge sums of money in repair and maintenance if not properly prevented. Thus, steel industries have employed galvanizing methods to prevent corrosion such as the hot-dip galvanization where the steel is dipped in molten zinc bath. However, the hot-dip galvanizing has been reported to reduce the fatigue strength which leads to premature cracking of the steel structure [38, 40]. To reduce the heating effect on the steel structure, improved methods such as the physical vapour deposition (PVD) of zinc on the steel substrate has been introduced, as seen in figure 1.1.
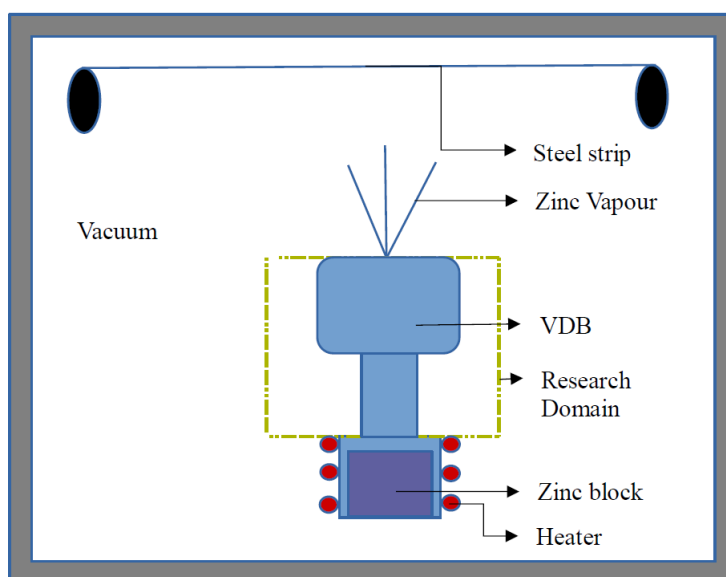
Figure 1.1: Schematic of the physical vapour deposition of zinc on steel strip showing the domain under study.

In Tata steel, zinc block is melted and vapourised with a heating element, the produced zinc vapour is then directed with a vapour distribution box (VDB) and after it leaves the nozzles is deposited on a moving steel strip just as in the schematic of figure 1.1. This physical deposition process is able to produce zinc coatings of micrometer

1

thickness with the aim of achieving the desired surface characteristic composition and aesthetics necessary for the business. The process of depositing the zinc vapour takes place at temperature of around 1000^oC in vacuum, increasing the difficulty to carry out experiments with flow visualization and measurement in the vacuum chamber. This restricted the steel company to trial and error experiments based on the final galvanized steel. To improve on the current state of the art at Tata steel, understanding what actually goes on in the vapour distribution box and nozzles of the physical vapour deposition process becomes increasingly important.

1.2. Research Objectives

In other to achieve a uniform surface finish on the steel plates, minimize stray depositions on the wall of the vacuum chamber, reduce undesirable cluster of zinc deposits, and scale up the system, one must understand the behaviour of the flow in the PVD system. Thus, this thesis aims at:

1. Simulating the physical vapour deposition process at Tata steel with computational fluid dynamics in order to characterise and comprehend the behaviour of the zinc vapour flow in the vapour distribution box and nozzles.

2. Obtaining a high and uniform mass flow rate for an efficient line production and aesthetic surface appearance.

3. Avoiding droplets on the steel strip by studying the condensation zones in the VDB and nozzles.

Since computational fluid dynamics analysis would be used for this purpose, the research only focuses on the transport of the zinc vapour from the inlet of the VDB to the VDB exit nozzles as shown by the research domain in figure 1.1, where the continuum approach in fluid mechanics does not breakdown.

1.3. Outline

In chapter 2 of this report, the governing equations and the theoretical background on gas dynamics and vapour jet condensation are given. Chapter 3 describes the physical problem under consideration. Afterwards, the mesh study and simulations performed are shown in chapter 4. In chapter 5, the results on the behaviour of the flow field in the vapour distribution box, the mass flow rate and condensation zones are given. And finally, the conclusion and recommendation of these results can be seen in chapter 6.

2

Theory

In this chapter, we begin by introducing the relevant dimensionless numbers that govern the flow in the VDB and through the nozzles. Afterwards, the governing equations for fluid transport is described, and since we are looking at continuum fluids in the VDB and nozzles not rarefied expanded gas atoms after the nozzles, these equations hold true. Then the behaviour of compressible vapour flow is studied with some relevant relations. And finally, a review on vapour nucleation is given.

2.1. Dimensionless Parameters

Before we go further into the report, the important dimensionless numbers which describes the behaviour of the flow are introduced in this section.

The transport of compressible fluid in vacuum depends on the Knudsen number, the Mach number, and the Reynolds number. As the jet expands into low pressure, the length of the mean free path increases. It results in a reduction in intermolecular collisions. This reduces the process of energy and momentum exchange between atoms. When the mean free path is comparable to the characteristic dimension of the jet, the continuum regime ends and the jet enters the transition regime, where the CFD approach is unable to simulate the rarefied zinc vapour. Moreover, molecular dynamics of the rarefied gas flow has been an important topic of research [6, 9, 10, 23, 36, 37]. The continuum approximation is valid at the length scale L when the Knudsen number,

$$\mathrm{Kn} = l/L \tag{2.1}$$

is much less than unity of $\mathcal{O}(10^{-3})$, where l is the molecular mean free path, which is the average distance a gas molecule travels between collisions. A brief description of the ranges in Knudsen number and their respective governing equations can be seen in figure 2.1.

In compressible flows, the speed of sound in the flow becomes relevant and cannot be treated as infinite as in an incompressible flow scenario. The importance of compressibility for the high vapour flow can be assessed by considering the Mach number M, defined as

$$\mathrm{M} = U/a, \tag{2.2}$$

where U is a representative flow speed, and a is the speed of sound. The propagation of the thermodynamic quantity, sound, for a reversible process assumes that changes

3
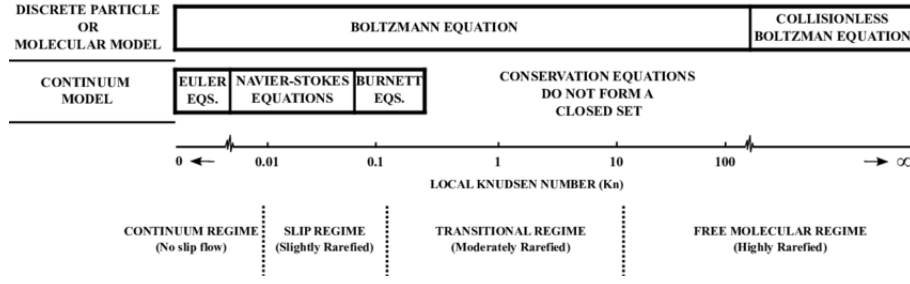
Figure 2.1: Flow regime classificatiomn and Knudsen number limits [8].

in density, pressure and temperature are infinitely small. This can be seen described below,

$$a^2 = (\partial p / \partial \rho)_s = \gamma R T. \tag{2.3}$$

Here, the subscript s signifies that the partial derivative is taken at constant entropy, because sound propagation is a reversible adiabatic process. Here p, ρ, γ, R, T represent the pressure, density, specific heat ratio, gas constant, and temperature of the flow respectively. From kinetic gas theory, the specific heat ratio for the monatomic gas,

$$\gamma = \frac{f+2}{f}, \tag{2.4}$$

depends only on the degree of freedom, f [11].

At M = 1, the Reynolds number at the nozzle called critical is given by,

$$\mathrm{Re}_* = a \rho_* d_* / \mu_*. \tag{2.5}$$

This critical Reynolds number alongside the ratio of nozzle outlet stagnation pressure, P_o, and the background pressure, P_H, describes the kind jet that leaves the nozzle - from continuum to rarefied jets, and viscously dominated to turbulent hypersonic jets [32].

2.2. Governing Fluid Equations

The principles governing fluid mechanics are the conservation laws for mass, momentum, and energy. These conservation equations which are derived by Kundu et al.[26, chapter 4] are used to describe the flow in the vapour distribution box. In analyzing fluid flow phenomena, attention is focused on what happens at the macroscopic rather than the microscopic scale. It is also assumed that the fluid is a continuum, so that its physical and flow properties are defined at every point in space. Since the flow in the VDB may be subsonic in most parts and supersonic in the nozzles or viscous dominated very close to walls, it is difficult to classify the flow and thus choose an appropriate solver for the transport equations. This numerical categorization is translated into the following: parabolic flows that are affected by previously computed values in the domain, elliptic flows by both upstream and downstream locations, and hyperbolic flows supporting discontinuities in the solution, e.g., shock waves [26, 31], as can be seen in figure 2.3.

The continuity, momentum and energy conservation equations are described below. The continuity equation in (2.6) gives the balance of mass going in and out of the control volume considering varying density.
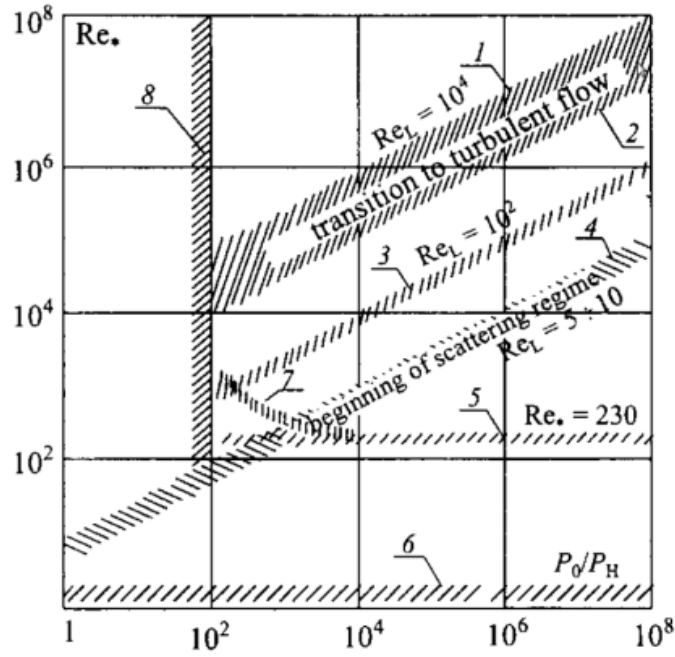
Figure 2.2: Flow regimes after the sonic nozzle. 1 - turbulent flow out of jet core; 2 - laminar flow; 3 - transition to a rarefied flow; 4 - transition to a scattering regime; 5 - existence of hypersonic flow in the jet core; 6 - effusion flow in the nozzle; 7 - violation of scaling law pressure ratio; 8 - existence of a cylindrical structure of jet behind the initial section at $P_o/P_H < 100$ are shown [32].
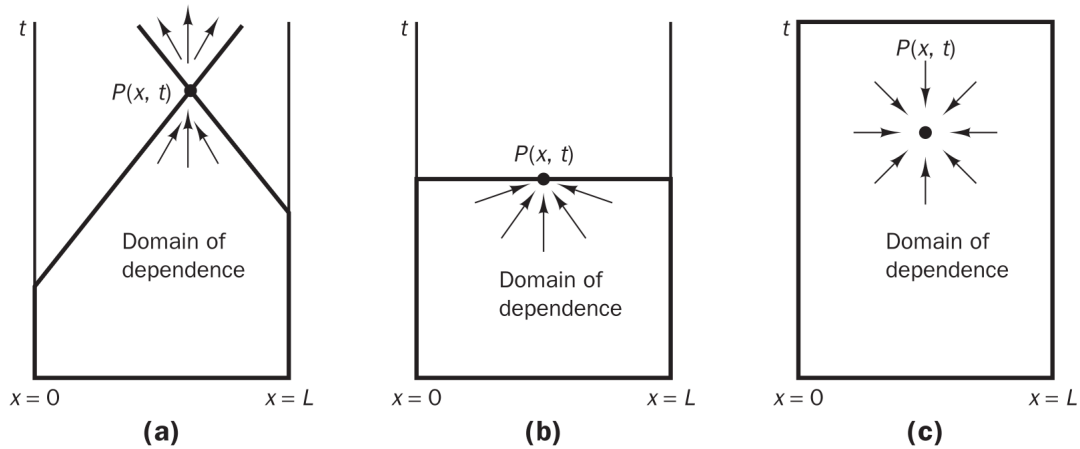
Figure 2.3: Domain of dependence for the (a) hyperbolic, (b) parabolic and (c) elliptic problems [44]. For example, Transient and supersonic flows are hyperbolic, boundary layer flows are parabolic, and irrotational flow of an incompressible fluid are elliptic.

$$\frac{\partial \rho}{\partial t} + \nabla \cdot (\rho \mathbf{v}) = 0, \tag{2.6}$$

where ρ is the density of the fluid and $\mathbf{v}$ is the velocity of the flow. The first term is the temporal term and second term is the divergence of mass-density flux $\rho \mathbf{v}$. The momentum equation in (2.7) below is developed from Newton's second law which balances the surface forces on the control volume ignoring the body force.

$$\frac{\partial \rho \mathbf{v}}{\partial t} + \nabla \cdot (\rho \mathbf{v} \mathbf{v}) = -\nabla P + \nabla \cdot [(\mu(\nabla \mathbf{v} + (\nabla \mathbf{v})^T)] + \nabla \lambda \nabla \cdot \mathbf{v} + \rho \mathbf{g}, \tag{2.7}$$

where μ is the dynamic viscosity and $\lambda = -\frac{2}{3}\mu$. To the left of (2.7) we have the temporal and convective terms and to the right, there is the pressure gradient term which represents the hydrostatic stress on the control volume while the other terms represent the viscous stress. The conservation equation of the total energy in the system is,

$$\frac{\partial \rho e}{\partial t} + \nabla \cdot (\rho e \mathbf{v}) = \nabla \cdot \mathbf{q} + [\nabla \cdot (\mu(\nabla \mathbf{v} + (\nabla \mathbf{v})^T) + \nabla \cdot \lambda(\nabla \cdot \mathbf{v})]\mathbf{v} - \nabla \cdot (P\mathbf{v}) + \rho \mathbf{g} \cdot \mathbf{v}, \tag{2.8}$$

$\mathbf{q}$ is heat flux through the surface of the control volume, the total energy in the control volume is $e = \hat{u} + \frac{1}{2}\mathbf{v} \cdot \mathbf{v}$, where $\hat{u}$ is the specific internal energy. The term in the square bracket on the right is the viscous dissipation term. The relation between density, pressure, and temperature is defined using the equation of state. Real gases most closely approximate ideal gas behaviour at high temperatures and low pressures which is due to the minimal effect of the intermolecular attraction. And thus the ideal gas equation of state is described as,

$$\rho = \frac{P}{RT} = \psi P, \tag{2.9}$$

where the compressibility is $\psi = \frac{1}{RT}$.

2.3. Gas Dynamics

In this section, we introduce the gas dynamics of monatomic metallic vapour as described in [26, chapter 15]. Some basic equations expressing the relations between the the flow variables and Mach number are mentioned. To understand how the speed of sound enters the compressible flow equations in the previous section, assumptions to simplify these equations are made. Let us consider a stationary adiabatic flow that non-isentropic effects such as viscous dissipation, thermal conduction, radiative energy transfer, chemical reactions, phase change, and shock waves are neglected. The energy equation (2.8) reduces to the following simplified Bernoulli equation for fluid with low density, hence neglecting the effect of body force;

$$\frac{v^2}{2} + h = constant, \tag{2.10}$$

where the constant in the r.h.s assumes different values for different streamlines, and $h = e + p/\rho$ is the specific enthalpy. For a variation of (2.10), with a change in enthalpy $dh = c_p dT$, the equation reduces to,

$$d\left(\frac{v^2}{2}\right) + c_p dT = 0, \tag{2.11}$$

and

$$c_p = \gamma c_v = c_v + R = c_p/\gamma + R. \tag{2.12}$$

Integrating (2.11) between two distinct points of the flow field and substituting the expression for c_p in (2.12), we obtain,

$$\frac{v^2}{2} - \frac{v_o^2}{2} + \frac{\gamma}{\gamma - 1}R(T - T_o) = 0. \tag{2.13}$$

Using the Mach number relation in (2.2), the first relation for the isentropic compressible fluid flow is derived,

$$a = a_o \frac{\left(1 + \frac{\gamma - 1}{2} M_o^2\right)^{1/2}}{\left(1 + \frac{\gamma - 1}{2} M^2\right)^{1/2}}.$$
(2.14)

(2.14) shows the speed of sound relation between two points in the VDB. A similar relation for temperature is derived using (2.3), and for pressure and density it can be derived using the isentropic relation with temperature,

$$p = p_o \left(\frac{T}{T_o}\right)^{\frac{\gamma}{\gamma - 1}}, \quad \rho = \rho_o \left(\frac{T}{T_o}\right)^{\frac{1}{\gamma - 1}}.$$
(2.15)

2.4. Solving the Transport Equations

Since the flow being considered goes across a range of subsonic inside of the VDB, the sonic in the nozzle, and afterwards supersonic during expansion after the nozzle, it is ideal to look at different solution methods for fluid flow. Hence in this chapter, the pressure and density based solvers are explained, with more emphasis on pressure based solvers as compared to density based solvers. Since our domain interest does not include the expansion region of the vapour flow, particle based simulation methods are not considered in this thesis.

2.4.1. Pressure Based Solver

According to Uroič et al.[43], to solve the transport equation, a compressible pressure equation is derived using the equation of state, continuity and momentum equation. Since the density depends on pressure and temperature, $\rho = \rho(P, T)$ the change in density over time is as follows,

$$\frac{\partial \rho}{\partial t} = \frac{\partial \rho}{\partial P} \frac{\partial P}{\partial t} + \frac{\partial \rho}{\partial T} \frac{\partial T}{\partial t}.$$
(2.16)

The second term introduces a source term dependent on the rate of change of temperature, allowing for a general polytrophic state change. And substitution of the equation of state, $\psi = \frac{\partial \rho}{\partial P}$ into the first term on the right of (2.9) would lead to the derivation of the pressure equation. The momentum equation is partially discretised as

$$a_p^{\mathbf{v}} \mathbf{v}_p = \mathbf{H}(\mathbf{v}) - \nabla P,$$
(2.17)

where

$$\mathbf{H}(\mathbf{v}) = \mathbf{r} - \sum_N a_N^{\mathbf{v}} \mathbf{v}_N.$$
(2.18)

The terms $a_p^{\mathbf{v}}$ and $a_N^{\mathbf{v}}$ represents the coefficients of the central and neighbouring nodes of the discretised domain respectively, and $\mathbf{r}$ represents the source term which is a result of the boundary condition.

The substitution of the velocity in the divergence term of the continuity equation (2.6) yields

$$\nabla \cdot (\rho \mathbf{v}) = \nabla \cdot [\rho (a_p^{\mathbf{v}})^{-1} \mathbf{H}(\mathbf{v})] - \nabla \cdot [\rho (a_p^{\mathbf{v}})^{-1} \nabla P],$$
(2.19)

and from equation of state $\rho = \psi P$, so (2.19) becomes

$$\nabla \cdot [\rho(a_p^{\mathbf{v}})^{-1}\mathbf{H(v)}] = \nabla \cdot \psi P[(a_p^{\mathbf{v}})^{-1}\mathbf{H(v)}], \tag{2.20}$$

thus the final form of the compressible pressure equation is as follows

$$\frac{\partial \psi P}{\partial t} + \nabla \cdot [\psi(a_p^{\mathbf{v}})^{-1}\mathbf{H(v)}P] + \nabla \cdot [\rho^o(a_p^{\mathbf{v}})^{-1}\nabla P] = 0, \tag{2.21}$$

where ρ^o is the previously obtained density solution. The second term of the pressure equation represents the convective effects and is responsible for the appearance of shocks and the third term is the pressure Laplacian term.
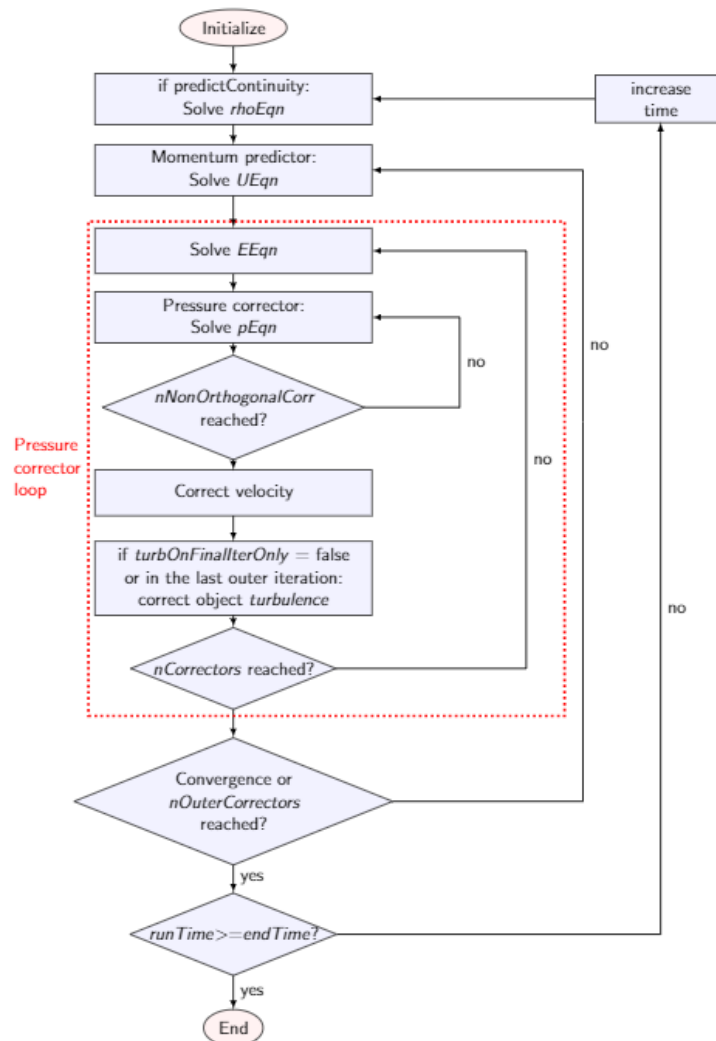
Figure 2.4: Flow chart of the sonicFoam solver.

   The momentum and derived pressure equation in (2.21) are then solved using the PIMPLE algorithm which combines the SIMPLE (Semi-implicit Method for Pressure Linked Equations) algorithm and PISO (Pressure Implicit with Splitting of Operators) algorithms as seen in figure 2.4. To reduce the number of iterations the continuity equation is solved first for every time step, if predictContinuity is true. After calculation of the momentum predictor, the PISO loop is called and begins by solving the energy equation. Then the pressure equation is solved *nNonOrthogonalCorr* times, for low mesh quality. In the last non-orthogonal correction loop, the velocity is corrected with contribution due to pressure correction and density variation. If *turbOnFinalIterOnly* is true, the objects turbulence is updated after the pressure corrector loop. But for the PVD process, no turbulence model is solved. The whole process is repeated until convergence or *nOuterCorrectors* is reached. Afterwards the time is increased by one time step as long as *runTime* is less than *endTime* [45].

2.5. Nucleation of Vapour Jet Flows

Since condensation is an important part of the PVD process, a brief review of the metal vapour nucleation is given below. Droplets on the steel substrate has been a lingering problem for Tata Steel. In the PVD system being modelled, a heating system is used to evaporate the zinc melt, and the evaporated zinc vapour is directed through the vapour distribution box (VDB) where it is pushed out through nozzles onto a steel strip as shown in figure 1.1. Cluster formation can occur at different parts of the setup. The zinc vapour faces a sudden expansion after leaving the nozzles and condenses as a result of the drop in temperature. Apart from the expansion after the nozzles, there can be cluster formation inside of the VDB if the thermodynamic state of some regions are in the liquid phase of the zinc phase diagram. The uneven clusters could also be as a result of the interaction of zinc atoms leaving through different nozzles. Parameters like the nucleation rate, cluster radius and number density are the best suited objective functions for nozzle optimization process, and could describe the degree of droplet formation in the expansion region of the jets [1, 17]. Bayazitoglu et al. [4] worked on an analytical and experimental study of nucleating zinc vapour in a converging nozzle and a sudden increase in pressure and temperature near the end of the nozzle was observed due to the latent heat required for particle growth and nucleation. Varying the nozzle length, larger particles were observed for longer nozzles. These large particles were also observed for higher initial vapour pressures. Giordano et al.[14] optimized a quasi-1D wet-steam nozzle using a moment method to describe evolution of liquid droplets and concluded that the optimal nozzle has a smaller exit area, which corresponds to a higher pressure at the exit and so a lower wetness fraction, with a similar study carried out by Keisari et al. [25]. Nucleation and condensation kinetics of zinc vapour in a laval nozzle was studied to predict the size distribution of the particles created at every position along the nozzle axis [24]. Tschudi et al. [42] used CFD to compare the presence and absence of steady nucleating and condensing flow in a laval nozzle.

3

Case Setup

In this chapter the geometry and boundary conditions are discussed. Finally, we look at the thermophysical properties used to describe the flow.

3.1. Geometry of the Vapour Distribution Box

The complete VDB geometry is shown in figure 3.1, with specifications from Tata steel. This set-up consists of; the vertical inlet channel, the long lateral VDB pipe, the nozzle connected to this VDB pipe,and the vacuum box. The zinc vapour flows in the positive y-direction from the inlet channel via the nozzles to the vacuum box.
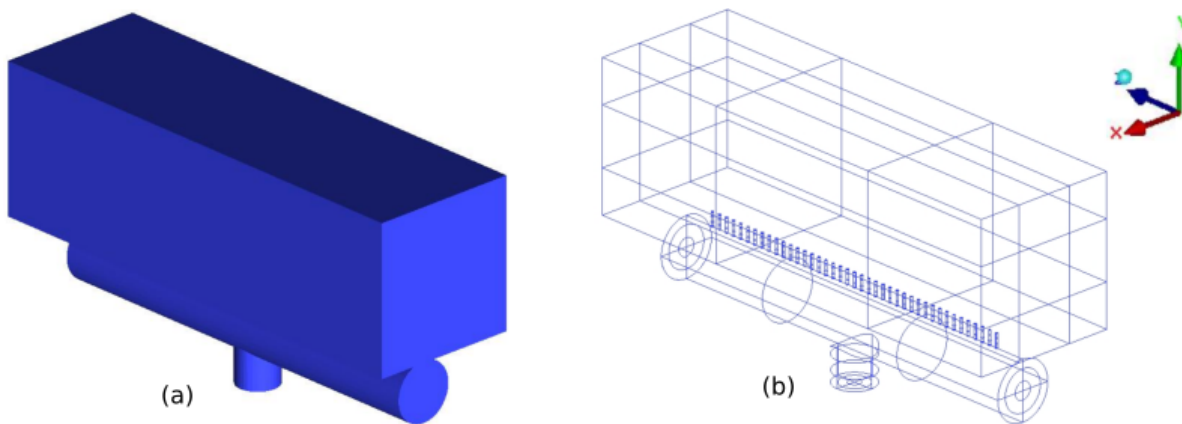
Figure 3.1: Surface and skeletal vapour distribution box geometry respectively.

3.2. Boundary Conditions

Below are the list of boundary conditions for the VDB boundary parts of figure 3.2. For the inlet, a total pressure of 5040 Pa is set, which is the zinc vapour pressure at 943.15 K temperature. Zero gradient velocity is set at the inlet, indicating no change in velocity across the inlet face. At the outlet, four outlet pressures are simulated (0.01 Pa, 1 Pa, 100 Pa, 1000 Pa). The temperature and velocity at the outlet are zero gradient except for back flow (bf). For the outlet velocity, zero velocity is given when back flow occurs, while 943.15 K is given for temperature. For the adiabatic wall, the pressure gradient

does not change and the components of the velocity are zero on the wall. A constant wall temperature is specified since the heat flux is zero. Zero normal gradient are given for all variables in the symmetry plane signifying that change in variable perpendicular to the symmetry face is zero. However, there could be changes in other direction. For the wall of the VDB, there is no change in pressure across the wall, and zero velocity for all components of the velocity. However, the temperature of 1273 K is given as the wall temperature.

Table 3.1: Overview of boundary conditions.

Type	Pressure	Velocity	Temperature
Inlet	5040 Pa	Zero gradient	943.15 K
Outlet	0.01 Pa, 1 Pa, 100 Pa, 1000 Pa	Zero gradient (no back flow)	Zero gradient (back flow = 943.15K)
Adiabatic Wall	Zero gradient	No slip	Constant wall temperature
Symmetry	Zero normal gradient	Zero normal gradient	Zero normal gradient
Wall of VDB	Zero gradient	No slip	Temperature: 1273 K
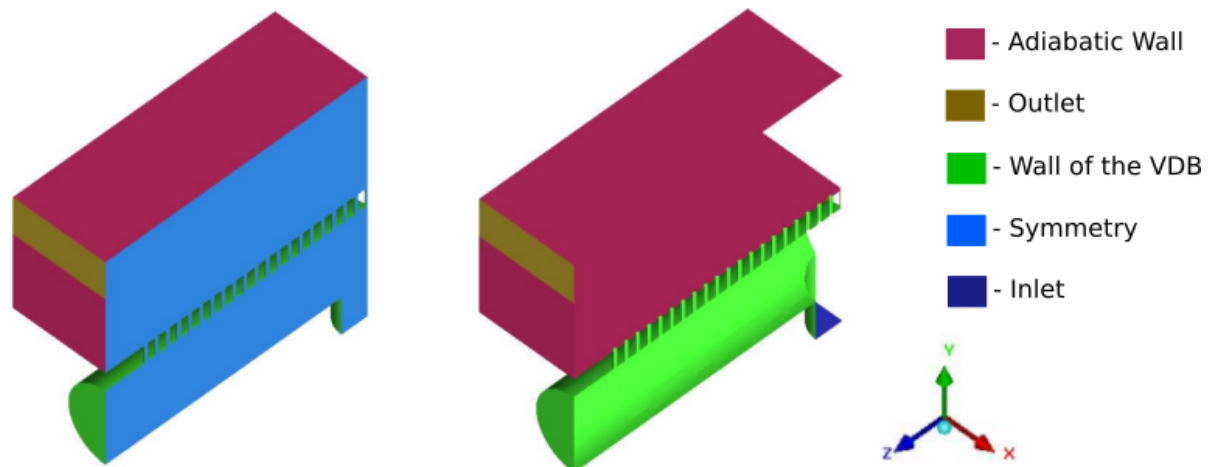
Figure 3.2: VDB boundary parts with and without symmetry patch. From the second figure without symmetry wall, the inlet patch can be seen. The outlet patch goes right round not on the symmetry patch, but only on the adiabatic wall.

3.3. Thermophysical Properties

In this section, the properties of zinc vapour that affects it transfer and storage of heat are given. Since the zinc vapour operates under low pressure and high temperature as described in the above section, the intermolecular forces weakens which enables the zinc vapour behaviour to closely approximate an ideal gas behaviour [27]. Thus the zinc vapour density is calculated using ideal gas equation in 2.9, with a molar mass of $M = 65.38 \, \text{kg/kmol}$.

The heat capacity for monatomic gases only depends on the translational modes in a three dimensional space, thus the molar heat capacity at constant volume is $C_v = \frac{3}{2}R$

and at constant pressure is $C_p = C_v + R = \frac{5}{2}R$ [33]. Therefore, the molar heats for zinc vapour becomes, $C_{v,zinc} = 20.79\,J/K/mol$ and $C_{p,zinc} = 318\,J/K/mol$ [7].

Due to the lack of viscosiy data for zinc vapour, we approximated the viscosity using a model by Fan et al. [13]. This derived data is curve fit with Matlab cftool to determine the Sutherland coefficients, A_s and T_s, relevant for implementation in openFoam. The curve fitting is shown in figure 3.3, and the Sutherland equation is given as [12]

$$\mu = \frac{A_s\sqrt{T}}{1 + T_s/T}. \tag{3.1}$$

with coefficients $A_s = 1.008 \times 10^{-6}\,Pa\,s\,K^{-0.5}$ and $T_s = 400.9K$.
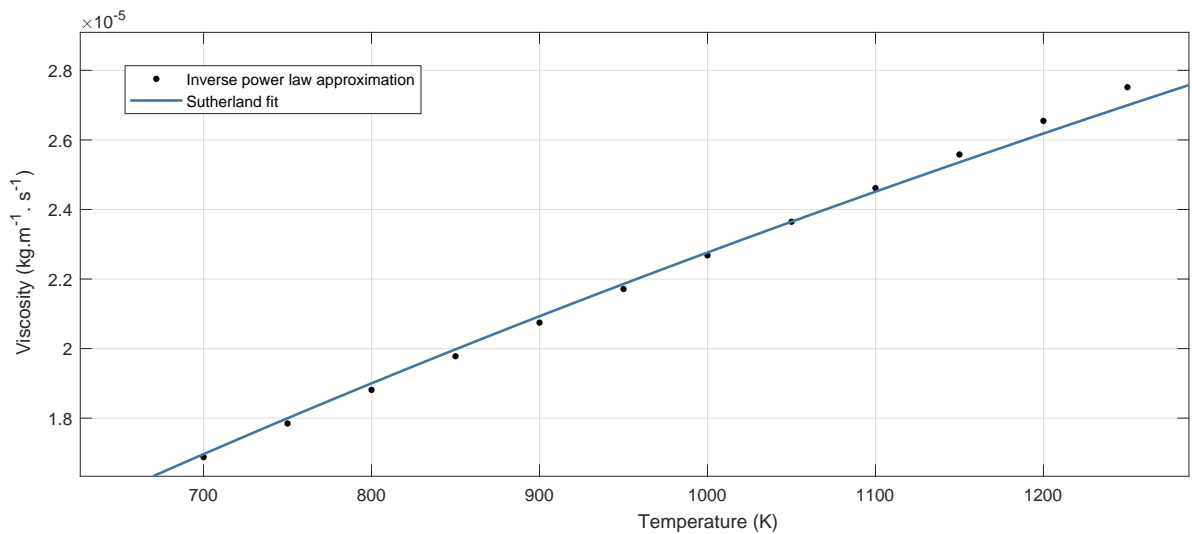
Figure 3.3: Plot of Sutherland fit.

4

Numerical Implementation

For this chapter, we discuss the meshing of the VDB, mesh refinement and o-grid meshing. The important mesh properties are also mentioned in this chapter - orthogonality, aspect ratio, skewness. A mesh independence study is carried out on three different mesh sizes. Finally, a brief discussion of the simulations performed and their convergence are given.
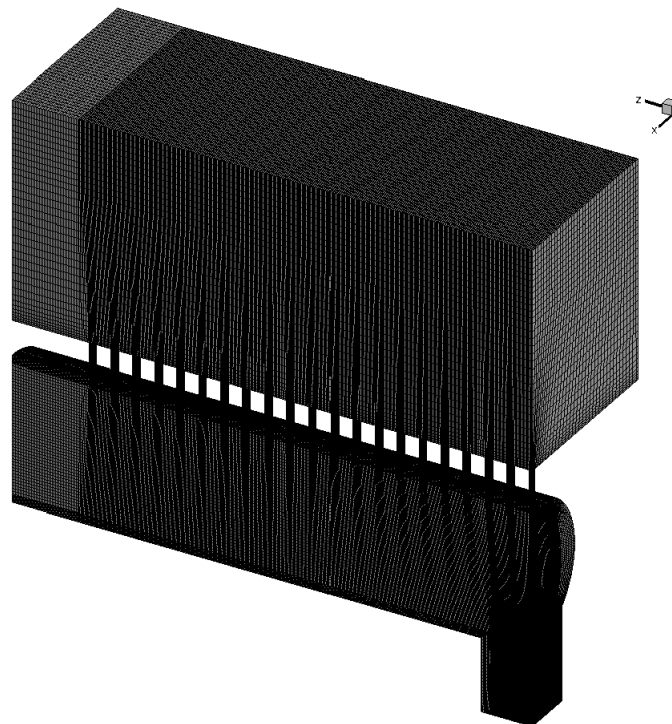
Figure 4.1: VDB Mesh with just over 2.3 million hexahedral control volumes. The darker regions show high cell density parts of the VDB.

4.1. Mesh

Meshing is an integral pre-processing part of any finite-volume based simulation since it determines the accuracy of solution and the required computation time. To resolve

the flow in the VDB geometry as in figure 3.2, the domain is sub-divided into approximately 2.3 million, non-overlapping control volumes or cells in figure 4.1. The governing equations described in chapter 2 are then solved for each of the control volumes. For an optimal mesh distribution, finer meshes are made close to the wall of the VDB and in the nozzles where the high gradients are expected, and coarser meshes are made where there are little changes from point to point.
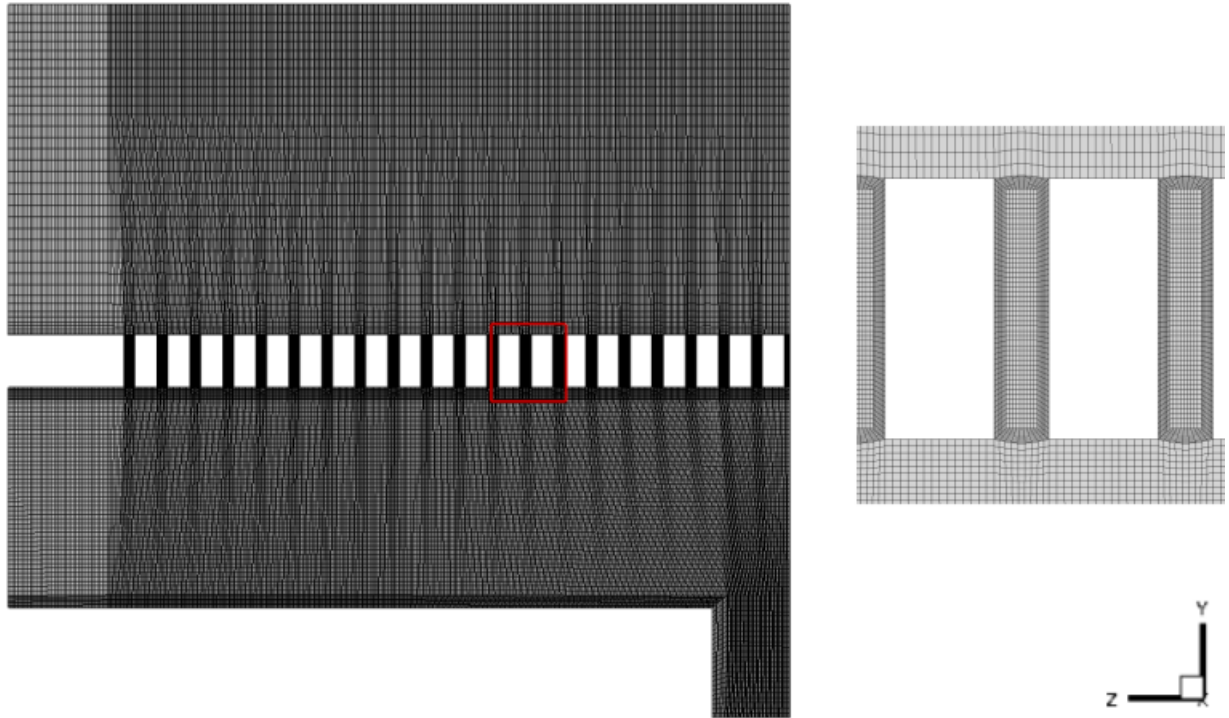
Figure 4.2: y-z plane of mesh showing an enlarged section of the nozzle refinement with 70 cells along the nozzle and 30 cells across. The darker regions in the VDB lateral channel and the vacuum box after the nozzle is due to the nozzle refinement, since all nodes are connected.

An enlarged section of the nozzle refinement is shown in figure 4.2. The meshes before the inlet of the nozzles are finer than the meshes after the nozzle with the zinc vapour flow in the positive y direction. In the nozzle, there is a finer mesh with approximately 30 cells across the nozzle - since the nozzle mesh is o-grid, hence the cells are not placed exactly parallel to the z-axis - than along the nozzle with 70 cells, since the zinc vapour flow experiences a steeper change across than along the nozzle. The most significant change occurs close to walls of the nozzles where the flow increases from zero velocity due to no slip condition to supersonic speeds at the center of the nozzle. For the PVD set-up, a structured meshing is implemented using ICEM CFD. This type of meshing requires that all cells are connected, and are known by its neighbouring cells and vice versa. Thus, there are no hanging nodes which is a mesh requirement in openFoam. Hence, you see darker regions before and after the nozzles due to the nozzle refinement.

In order to construct a structured mesh for the PVD set-up, the geometry is divided into different sections, commonly known as blocking. Different mesh techniques are then performed on the different blocks. For the VDB lateral channel, inlet channel and nozzles, an internal O-grid blocking is used to improve the angles in the blocked corners
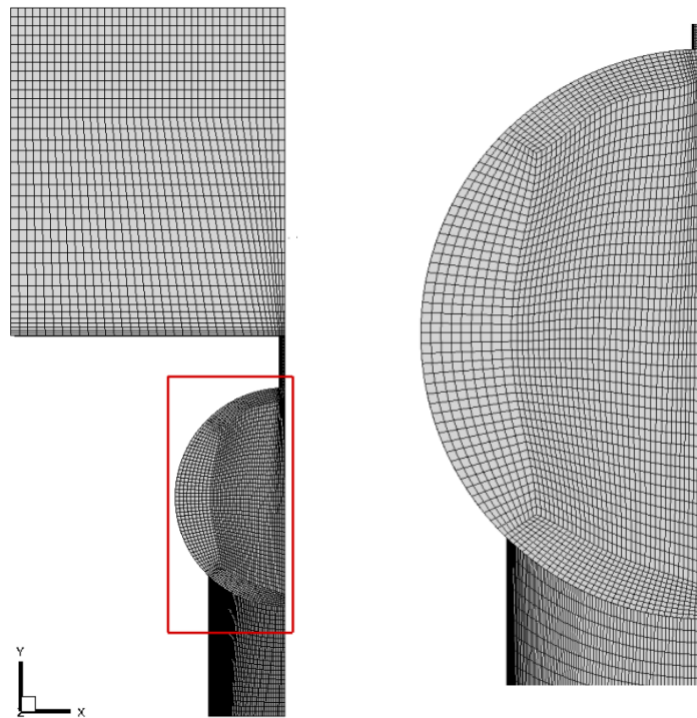
Figure 4.3: Side view of the mesh with 2.3 million cells. On the right: Enlarged section with O-grid meshing for cylindrical geometry.

like in figure 4.3. This meshing method on the cylindrical parts of the set-up produces low skewed mesh with orthogonal grids close to walls, thereby improving the overall mesh quality [3].

The quality of the mesh constructed is essential in achieving an accurate and stable CFD solution. To guage this quality, several criteria has to be met with regards to the type of mesh, skewness, non-orthogonality, aspect ratio. With several types of mesh available - tetrahedra, triangular prism and pyramidal meshes - the most suitable for openFoam simulation is the hexahedra mesh. Just being hexahedron does not signify a good mesh. The angles between the faces has to be approximately equal, which means the hexahedra mesh is less skewed, see figure 4.4. And the maximum internal face skewness for openFoam is four.
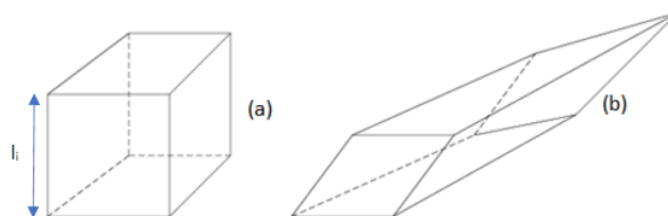
Figure 4.4: Hexahedron meshes with aspect ratio = $\frac{Min(l_i)}{Max(l_i)}$. (a) Low skewed mesh. (b) High skewed mesh.

The interaction of a control volume with its neighbouring control volumes is also important, which brings us to mesh non-orthogonality. The angle between the normal vector of the face of a parent cell and the vector connecting the center of the parent cell to its neighbouring cell should be as close to zero but not more than 70°. Very Low

mesh non-orthogonality - maximum of 5°- reduces the instability of the simulation and time of computation, since the explicit non-orthogonal correction added as the source term would not need to be computed [20–22]. Finally, the aspect ratio of the cells which determines the equality of the cell edge is essential. This is important because the coefficients in the matrix from the system of equations becomes irregular leading to an ill-conditioned matrix, since off-diagonal coefficients becomes excessively larger that the diagonal coefficients.

4.1.1. Mesh Independence Study

The discretisation error reduces with mesh size. In other words, the finer the mesh, the better the accuracy of the CFD simulation. Iterative methods are used to solve the large system of equations resulting from the refined meshes. However, the convergence rate of iterative methods rapidly reduces as the mesh is refined. Thus a compromise has to be reached between accuracy and computation cost. For the PVD set-up, three different mesh sizes are constructed as listed in table 4.1 with their various properties. To achieve the balance between computation cost and accuracy, a study is carried out on these meshes. An inviscid zinc vapour flow with an outlet pressure of 0.01Pa is simulated with the different meshes and the resulting mass flow rate from the nozzles in figure 4.5. The mass flow rate from the nozzles of mesh with the lowest size is overestimated
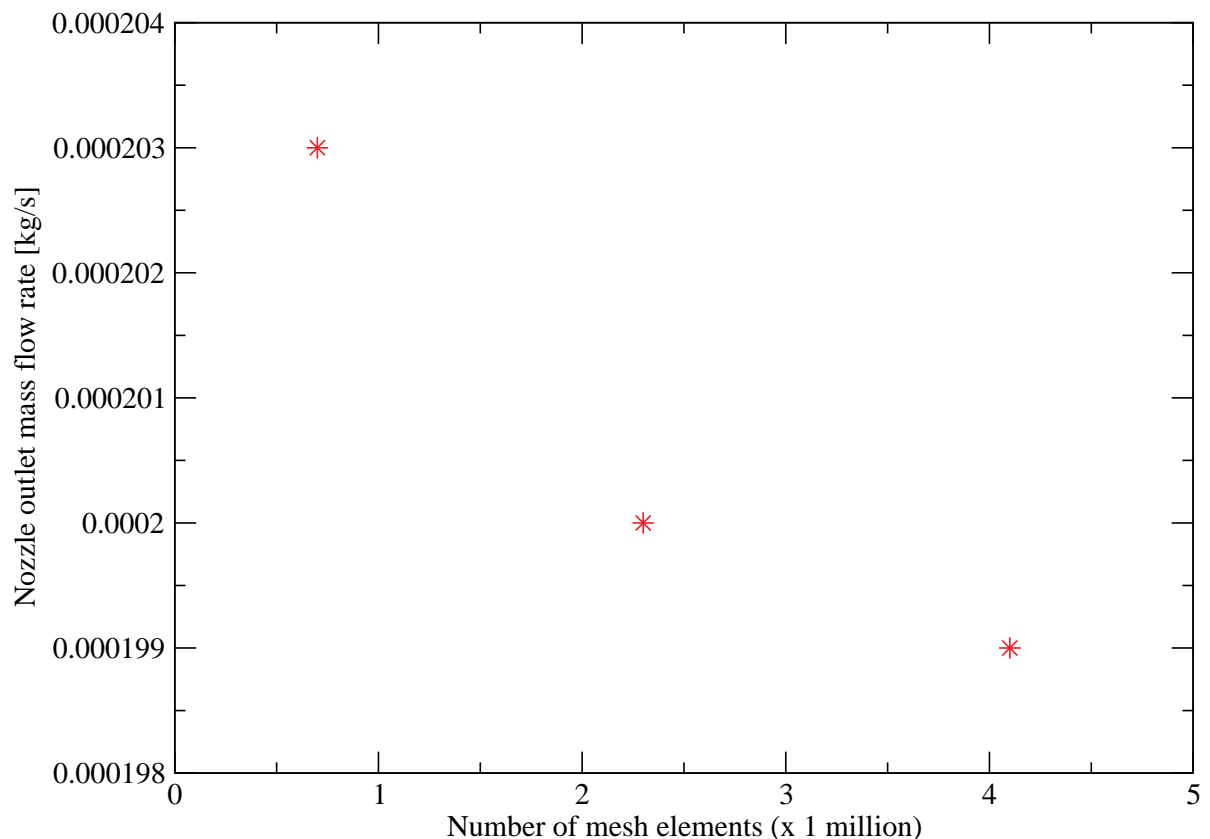
Figure 4.5: Total outlet mass flow rate from the nozzles for different mesh sizes of an inviscid case with 0.01 Pa outlet pressure.

as compared to the other two mesh sizes. With a deviation of around 1% from the mesh with 2.3 million cells. The mesh with 0.75 million cells seems good, however, for

simulations of higher outlet pressures, the mesh with 2.3 million cells produced a more accurate result since it was able to properly predict the unsymmetrical boundary layer in the nozzles affected by recirculation, see appendix A. The mesh with the 4.1 million elements gives the best estimation, but with a difference of 0.5% in mass flow rate prediction which required two extra weeks of computation time with twice the number of processors. Thus the medium mesh with 2.3 million cells was chosen for this thesis, with a computation time of around two weeks for 0.01 Pa outlet pressure simulation.

Table 4.1: Mesh properties for different number of cells.

	Mesh 1	Mesh 2	Mesh 3
No. of cells	754,528	2,323,528	4,075,388
Mesh Type	Hexahedra	Hexahedra	Hexahedra
Min cell volume [m^3]	1.25×10^{-12}	3.86×10^{-13}	3.86×10^{-13}
Max cell volume [m^3]	4.12×10^{-9}	1.37×10^{-9}	6.45×10^{-10}
Max aspect ratio	12.06	12.28	12.28
Max skewness	2.02	2.26	2.26
Avg. non-orthogonality	12.9°	12.5°	11.7°
Max non-orthogonality	62.0°	67.1°	67.4°

4.2. Simulations

For the CFD analysis of the PVD process at Tata steel, a pressure based solver in open-Foamv1806 is employed. Inviscid and viscid cases were simulated at different outlet pressures. For the simulation of the PVD process, the pressure based solver - sonic-Foam - proved to be stable because it was able to simulate the PVD process at different conditions. Since the zinc vapour flow in the inlet channel and VDB channel are below or close to the incompressible Mach number limit of 0.3 [29, 35], the sonicFoam solver was able to compute the pressure and velocity fields to a good degree of accuracy. The sonicFoam which solves for high speed flows obtained physical results in the nozzles. Since the PVD process is a high Peclet number flow process, upwind scheme was used for the divergent terms, hence, accuracy was not totally lost. This numerical discretisation scheme was stable while higher order schemes like van Leer was not. To also reduce numerical error, the set-up of 0.05m $\times$ 0.13m $\times$ 0.14m was divided into 2.3 million volumes. Computing six variables - Mach number, pressure, temperature and three components of the velocity - for each of this volumes took average of 2.5 weeks/case. An overview of all the simulated cases is shown in table 4.2.

4.3. Convergence

Due to the complexity of the problem, just achieving a very low residual of order 10^{-6} does not imply the simulation is converged. Before the results can be post-processed, the simulation has to reach a steady state. For the PVD process simulation, the mass flow rate at the inlet and outlet of the set-up are compared in time in figure 4.6. From this figure, around five thousandth of a second the simulation reaches steady state since the difference between the inlet and outlet mass flow rate is less than 1%. To ensure no

Table 4.2: Simulated converged sonicFoam cases.

VDB Case	Viscosity	Outlet Pressure [Pa]
1	Inviscid	1000
2	Inviscid	100
3	Inviscid	1
4	Inviscid	0.01
5	Viscid	1
6	Viscid	0.01

other spurious fluctuation in the mass flow rates would occur, the simulation is allowed to run for more than twice its settling time. To further investigate the effect of this fluctuations, the variables were averaged over time and the root mean square velocity is computed and show in appendix B.
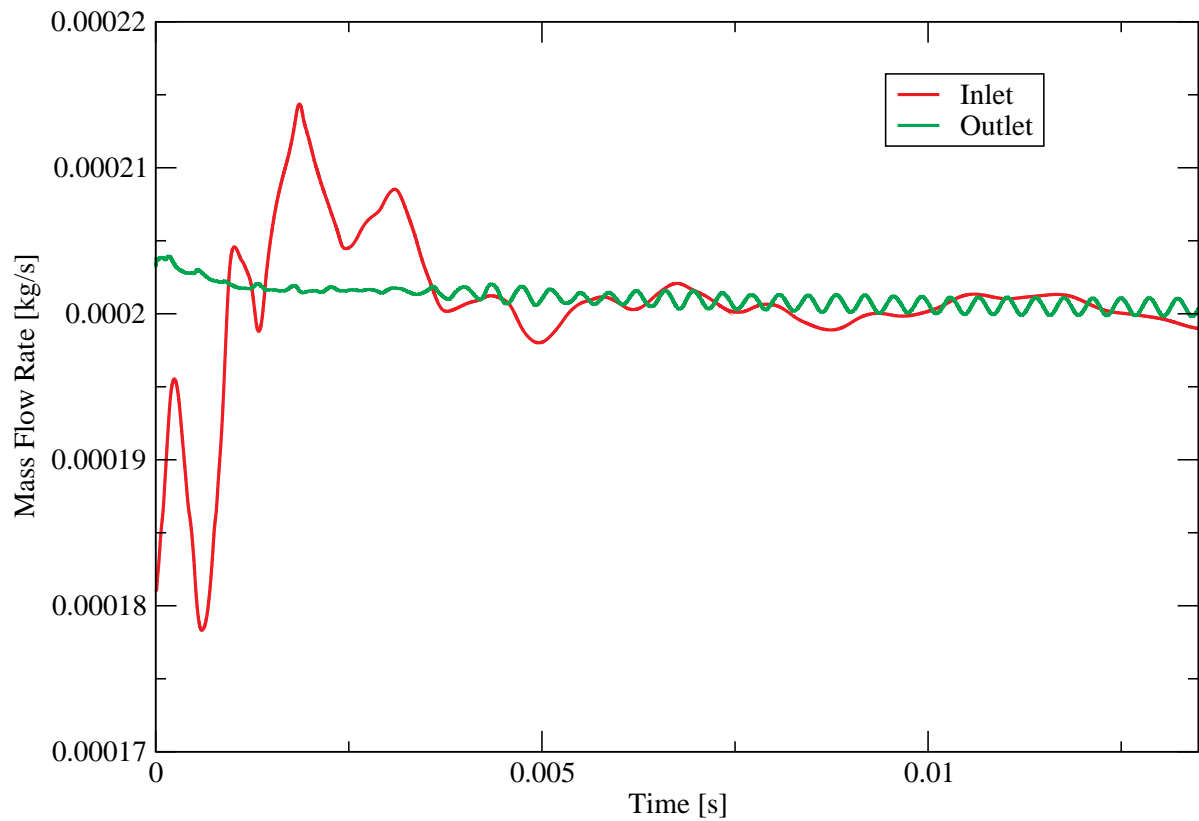

Figure 4.6: Mass flow rate convergence plot of the inlet and outlet patches for a viscid case with outlet pressure of 0.01 Pa.

5

Results and Discussions

To achieve a high and uniform mass flow from the nozzles, avoid condensation before the vapour reaches the steel, and minimise stray deposition, we need a good understanding of the flow inside the VDB and nozzles. Thus, the chapter explores the behaviour of the compressible zinc vapour flow for a viscid case with outlet pressure of 0.01 Pa except mentioned otherwise: Firstly, the flow through the whole system is described qualitatively. Then we focus on the recirculation in the VDB and its effect on the flow inside the nozzles. Afterwards the uniformity of the mass flow rate is analysed and compared with the experimental value provided by Tata Steel. Eventually, the regions with high tendencies of phase change are identified.

5.1. Flow Description in the PVD System

The flow in the PVD system is driven by the difference in zinc vapour pressure at the inlet and the outlet pressure close to vacuum in the positive y-direction. The zinc vapour flows through the inlet channel and experiences no-slip at the wall. The streamlines of the flow in the inlet channel follow a smooth path but circulate as it leaves the inlet channel into the larger lateral VDB channel in figure 5.1(b). The flow through this inlet channel impinges on the inner VDB wall directly opposite to the inlet face, some partially flows through the nozzles and the rest fills up the VDB. Due to the impingement, a pressure built up around the nozzles opposite the inlet face in figure 5.1(a). Thus a pressure difference between that region and the far end of the VDB causes more of the zinc vapour to flow laterally resulting in the irregular streamlines in the lateral VDB channel. Due to wall heating, the temperature in the VDB channel increases next to the walls in figure 5.1(c).

The pressure build up in the VDB forces the flow to accelerate through the nozzles up to supersonic speed. The accelerated flow in the nozzles is affected by the flow behaviour in the VDB channel described in the previous paragraph, and is looked in detail later in this chapter. After the acceleration of the zinc vapour through the nozzles, this compressible fluid is expanded into the region with near vacuum pressure ($P_{outlet} = 0.01$Pa). This results in supersonic underexpanded jets with a Mach number of around 3 in figure 5.1(d). During the expansion, a rapid speed up and decrease in temperature occur as shown in figure 5.1(b),(c). Further downstream, there is an increase in temperature and decrease of the Mach number, indicating that the flow shocks in front of the wall.
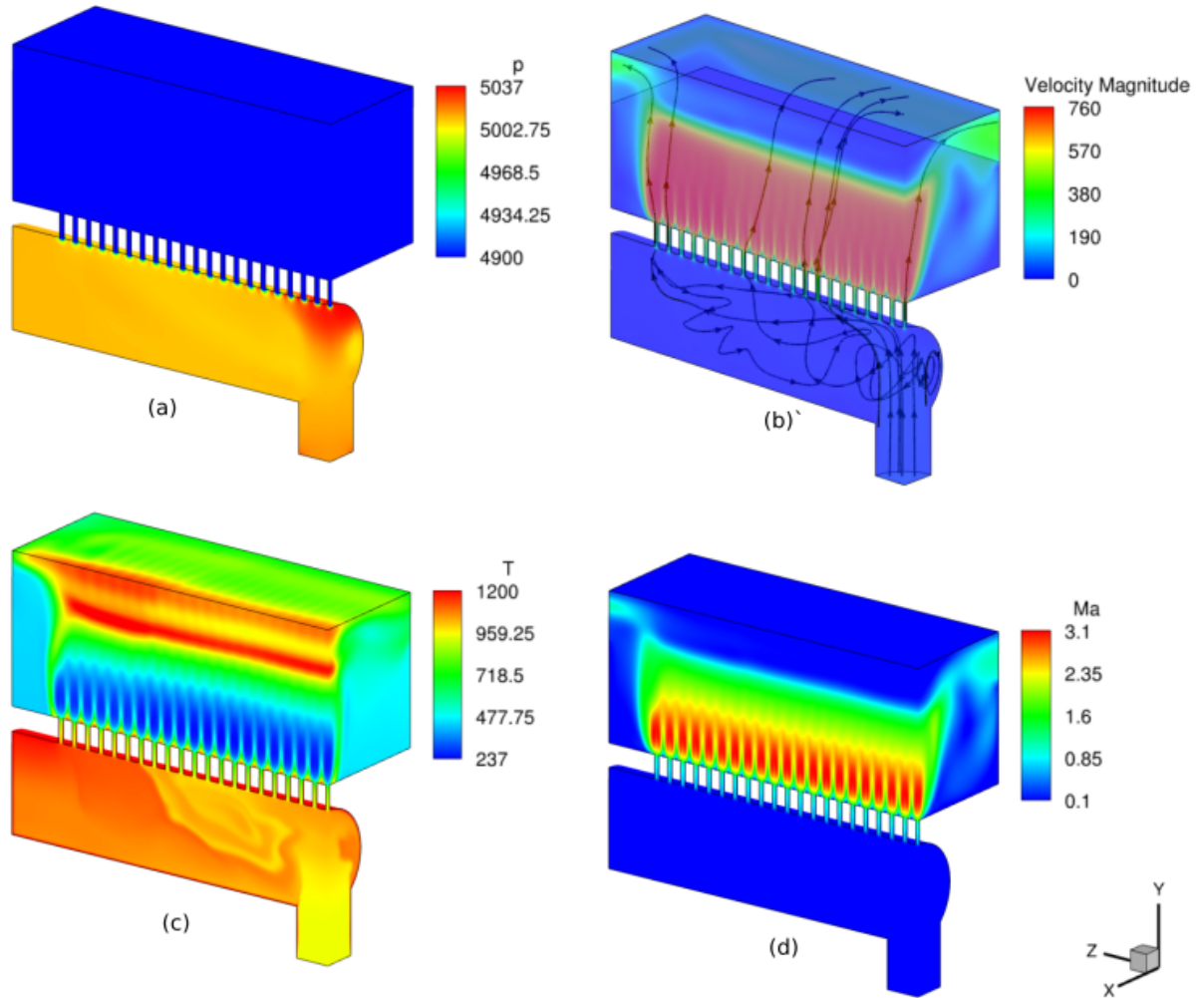
Figure 5.1: 3D contour of different flow properties in the PVD system. (a) Pressure in Pa. (b) Velocity magnitude in m/s with streamlines. (c) Temperature in K. (d) Mach number of the flow.

The flow phenomena in this expansion region do not describe the physics as the continuum assumption on which the CFD modelling is based breaks down due to the relatively high Knudsen number ($Kn = \mathcal{O}(10^{-1})$) [8], and the zinc vapour does not stick to the steel plate in the model. Thus, subsequent results in the expansion region is cut off.

Figure 5.2 shows 2D contour of pressure and temperature of the mid-plane through the longer axis of the set-up. For the pressure contour, apart from the high pressure region opposite the inlet face, there is a slightly lower pressure just around the corner as compared to the end of the VDB channel. This region of slight pressure drop with an irregular flow around the corner resulted in temperature recirculation zone in figure 5.2. Along the nozzles, there is a drop in pressure with a simultaneous drop in temperature.

Figure 5.3 shows the 2D contour of Reynolds number in the VDB using the lateral VDB channel diameter as the characteristic length. The Reynolds number is less than the critical Reynolds number for smooth pipe flow, Re = 2300 [34] in the lateral VDB channel, apart from the interconnecting region with the inlet channel. From the front view figure of the 2D contour, approximately five nozzles are affected by the high Reynolds flow from the inlet channel and are also affected by recirculation of zinc vapour

flow around the corner.
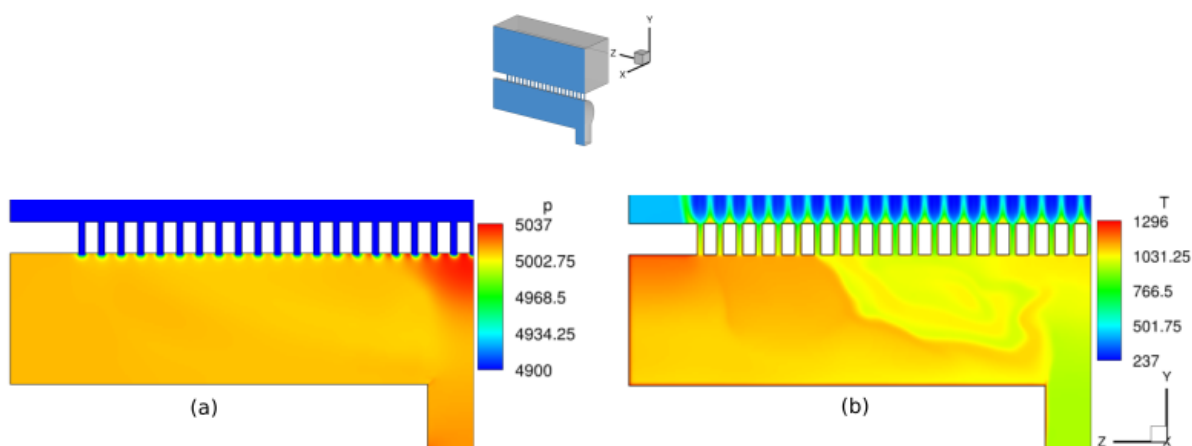
Figure 5.2: Mid-plane 2D contour of (a) Pressure, p (Pa) and (b) Temperature, T (K).
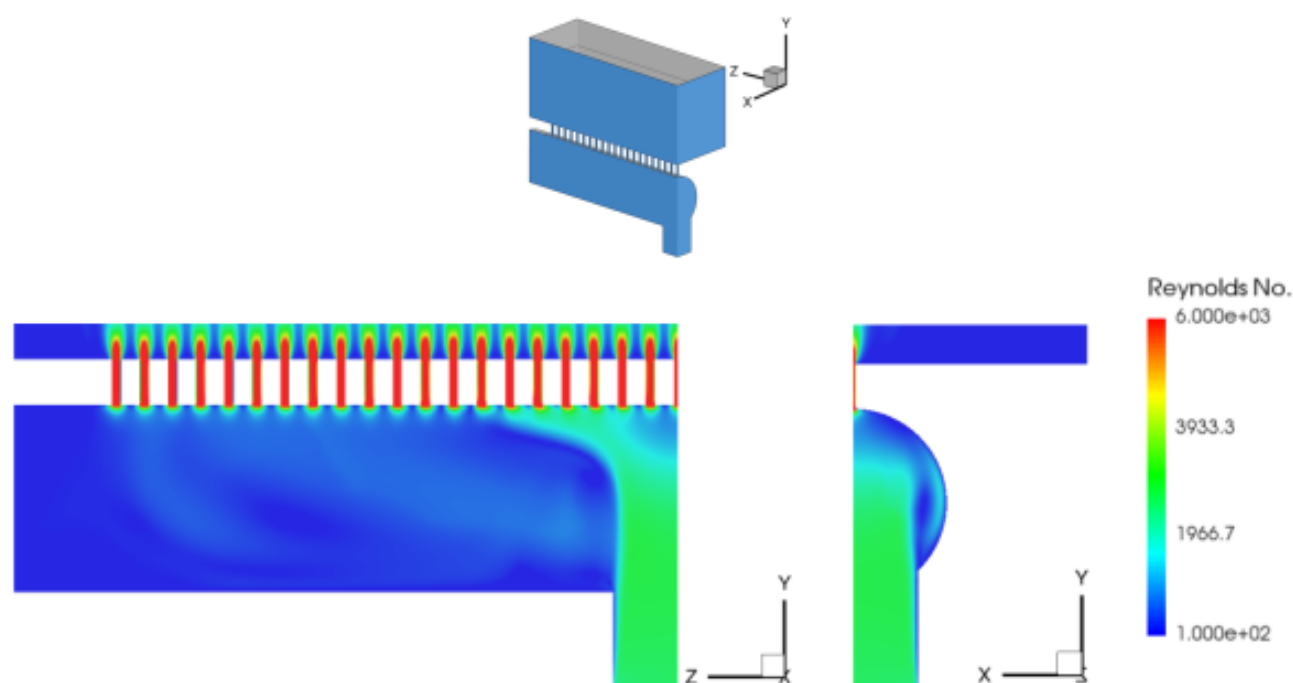
Figure 5.3: Front and cross-section view of the Reynolds number contour in the VDB and nozzles.

Close to the semi-circular wall of the cross-section view of the Reynolds contour in figure 5.3, a relatively high Reynolds number is attributed to another recirculation of the zinc vapour about a different axis as seen with the velocity stream lines in figure 5.1 (b). Since the lateral VDB channel diameter was used to compute this Reynolds number contour, the Reynolds number in the inlet channel and nozzles are overestimated by one and two orders of magnitude respectively. Thus, no turbulence model was used to predict the behaviour of the flow in this study.

For the Mach number contour in figure 5.4, the flow from the inlet channel of the VDB and the lateral channel is less than 0.3, thus the zinc flow in the VDB can be described using the incompressible fluid approach. As the flow accelerates through the
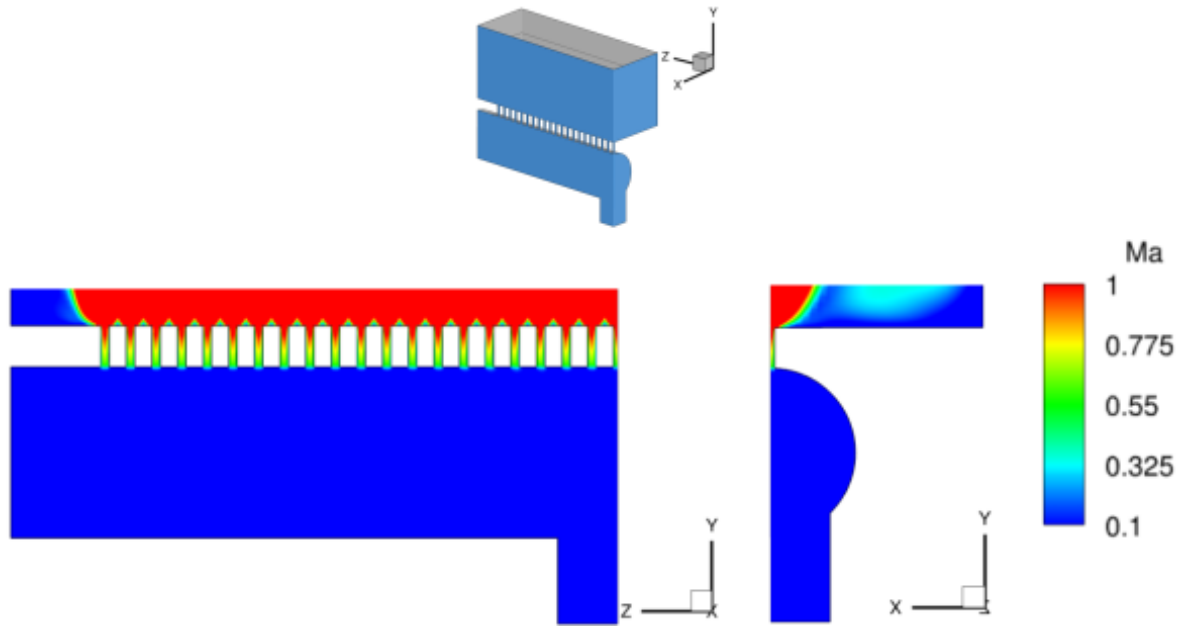
Figure 5.4: Rescaled Mach contour showing the position in the nozzles where the speed of the zinc vapour flow equalled the speed of sound in air.

nozzles, the speed of the zinc vapour flow equals the speed of sound in air and eventually exceeds this sound speed, making the zinc vapour flow supersonic. The zinc vapour flow approaches Mach one around the mid way through the nozzles.

5.1.1. Flow Field in the Vapour Distribution Box

To understand the zinc vapour flow in detail, we start by looking at the streamlines and vorticity on the y-z plane of the VDB in figure 5.5. The streamlines of the recirculating flow around the corner of the inlet channel is not fully captured on this plane. However, the vorticity around the corner on the y-z plane can be seen, and the nozzles are affected by this recirculation in figure 5.5 (b). The flow in the seventh nozzle which is affected by this flow irregularity is further studied later in this section. The streamlines also appear to be irregular in the lateral VDB channel as in the 3D case in figure 5.1(b), with another recirculation at the corner of the lateral VDB channel in figure 5.5 (a).

Before describing the flow profile at different locations, figure 5.6 helps with understanding the positions in the VDB and nozzles under analysis. Some terminologies used to describe the flow in the rest of the section is also labelled in this figure, and can be used as reference for understanding the flow description.

Temperature profile across three different nozzles at different locations is shown in figure 5.7. From the plot, the temperature profile for the seventh nozzle is the lowest around the center of the nozzle for the different nozzle locations. Close to the wall of the nozzles, a different behaviour is observed in the upstream part of the nozzle - diameter < 0.0005m - for the inlet temperature plots. Going from the inlet cross-section to mid and finally to the outlet, there is a significant drop in temperature for the three nozzles. There is also temperature drop along the seventh nozzle in figure 5.12(a).

For the pressure profile in figure 5.8(a), the effect of recirculating zinc vapour flow leaving the inlet channel around the corner is seen in the varying pressure levels at
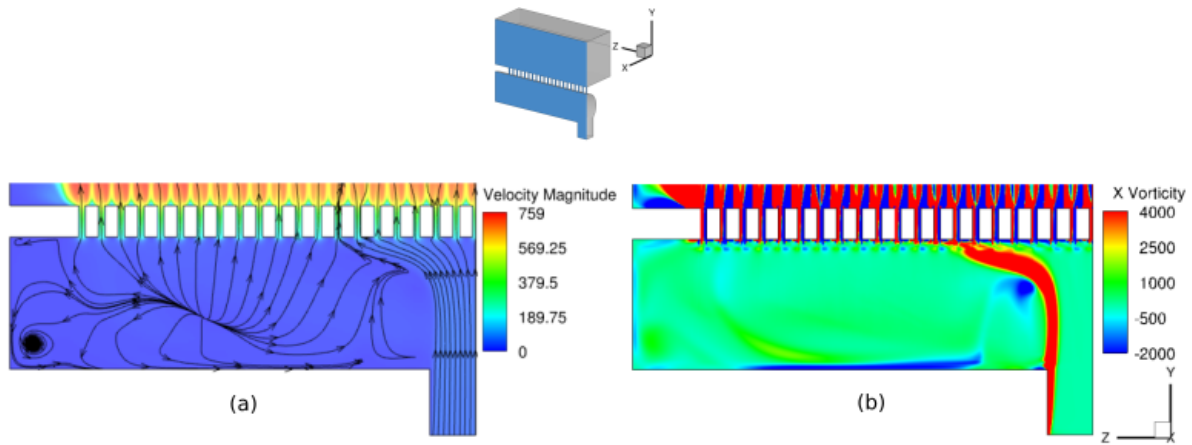
Figure 5.5: VDB velocity streamlines and vorticity.
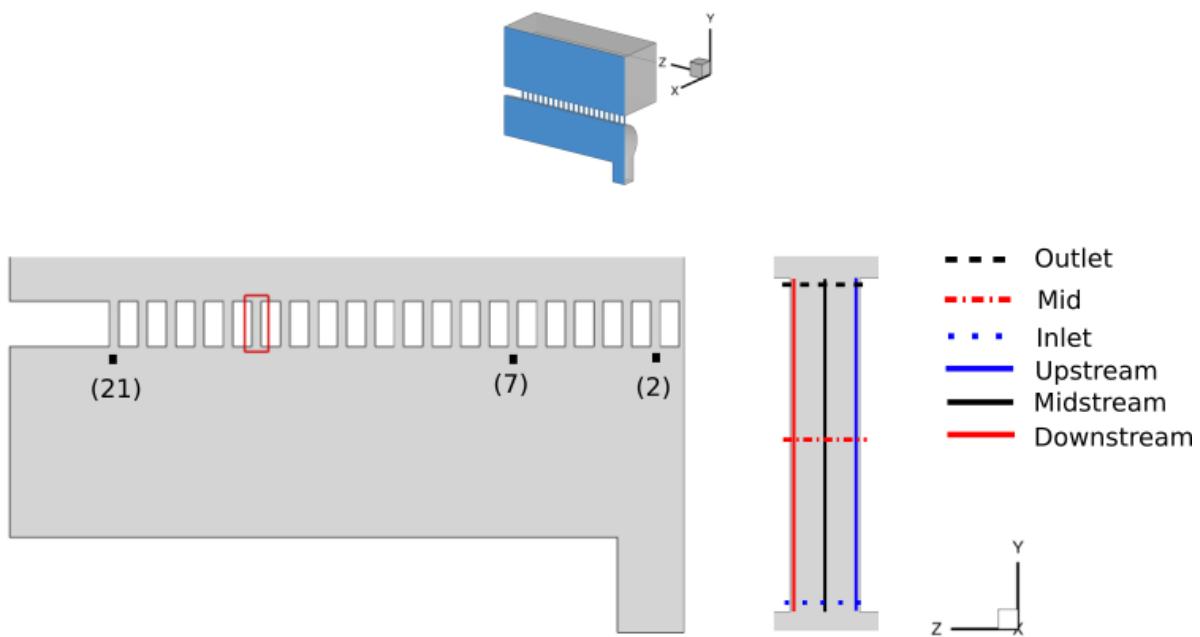
Figure 5.6: Plot locations for analysis on the y-z plane of the VDB. This is figure also shows a zoomed out part of the nozzle for reference on the locations of sample lines.

the upstream and downstream side of the nozzle. Since the zinc vapour speeds up as it recirculates and stagnates at the downstream wall - diameter > 0.0015m - of the seventh nozzle, high pressure is built up on that part of the nozzle as compared to the the other nozzles in figure 5.8(a). The reverse is the case for the upstream side of the nozzle, since the zinc vapour flow speeds up in other to balance mass and momentum. The same effect occurs in the second nozzle but is reduced. In Nozzle 21, there is a more symmetrical dumbbell shape because at the lateral end of the VDB, the flow is driven by only the difference in inlet and outlet nozzle pressure and not affected by recirculating flows. As the zinc vapour flows through the nozzle, the mid pressure flattens out with the pressure decreasing with distance from the inlet channel in figure 5.8(b). At the outlet pressure for the three nozzles, the pressure returns to a bell shape, figure 5.8(c), due to the supersonic expansion of the zinc vapour.

The velocity magnitude plot in figure 5.9 and Mach number plots in figure 5.10 are similar in shape since the Mach number is the ratio of the velocity magnitude with that of the speed of sound in the zinc vapour depending on the temperature distribution. From both plots, there is a speed up as the zinc vapour moves from inlet to outlet for the different nozzles. Around the mid section of the nozzle, the velocity of seventh nozzle is lowest but has approximately the same Mach number as the other nozzles studied. The velocity profile becomes more unsymmetrical as the zinc vapour flows from the nozzle inlet to outlet. This unsymmetrical nature of the profile is not observed in the Mach number plot, which is balanced out by the temperature field in the VDB. Moving to the wall of the nozzles, there is no significant difference in Mach number.
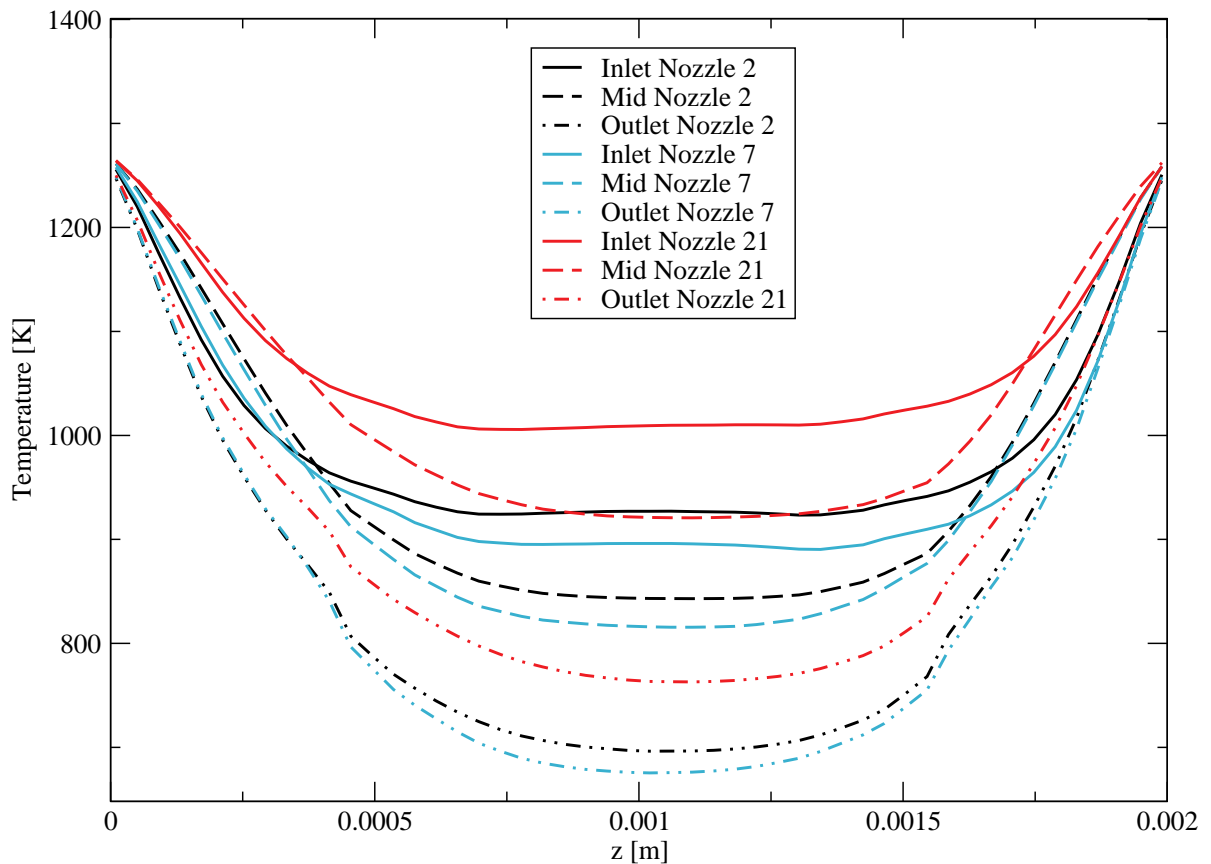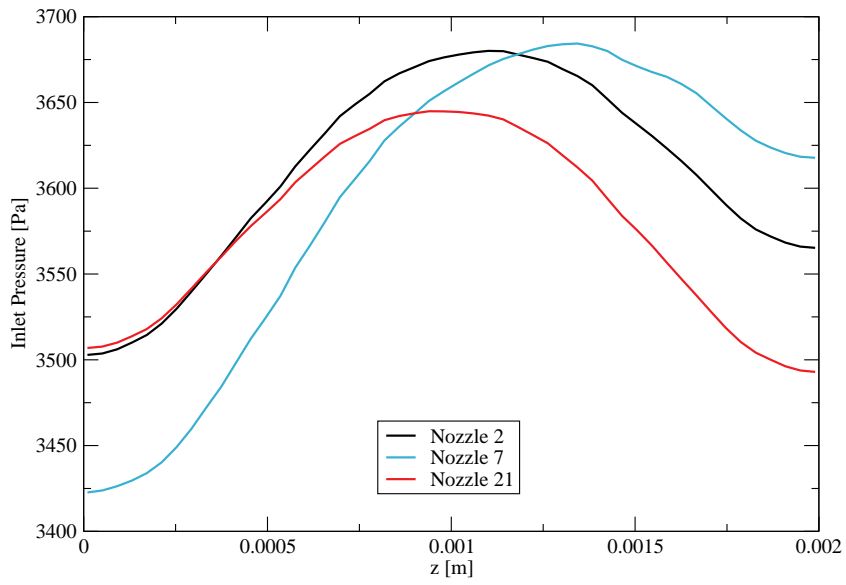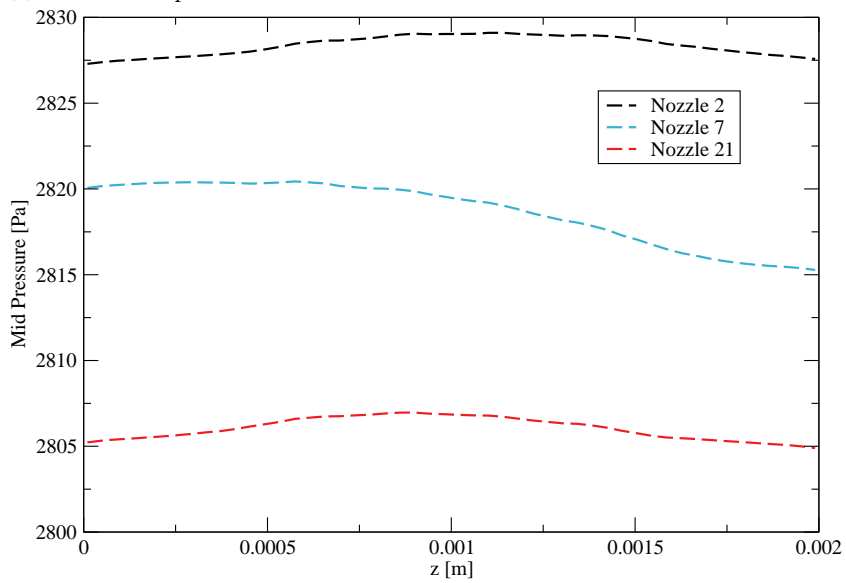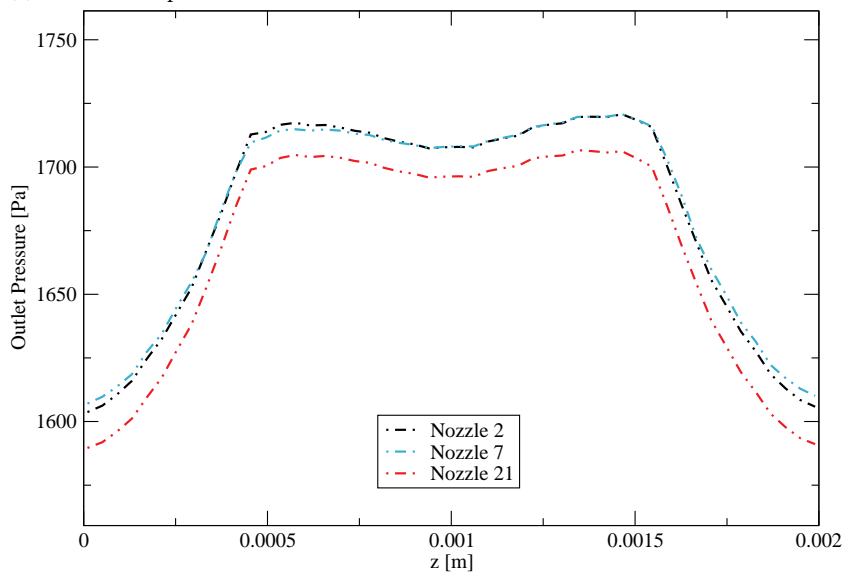

Figure 5.7: Temperature plot against the z-coordinate for different positions in the nozzle.

(a) Inlet Pressure plot.

(b) Mid Pressure plot.

(c) Outlet Pressure plot.

Figure 5.8: Pressure plot against z-coordinate for different nozzle positions.
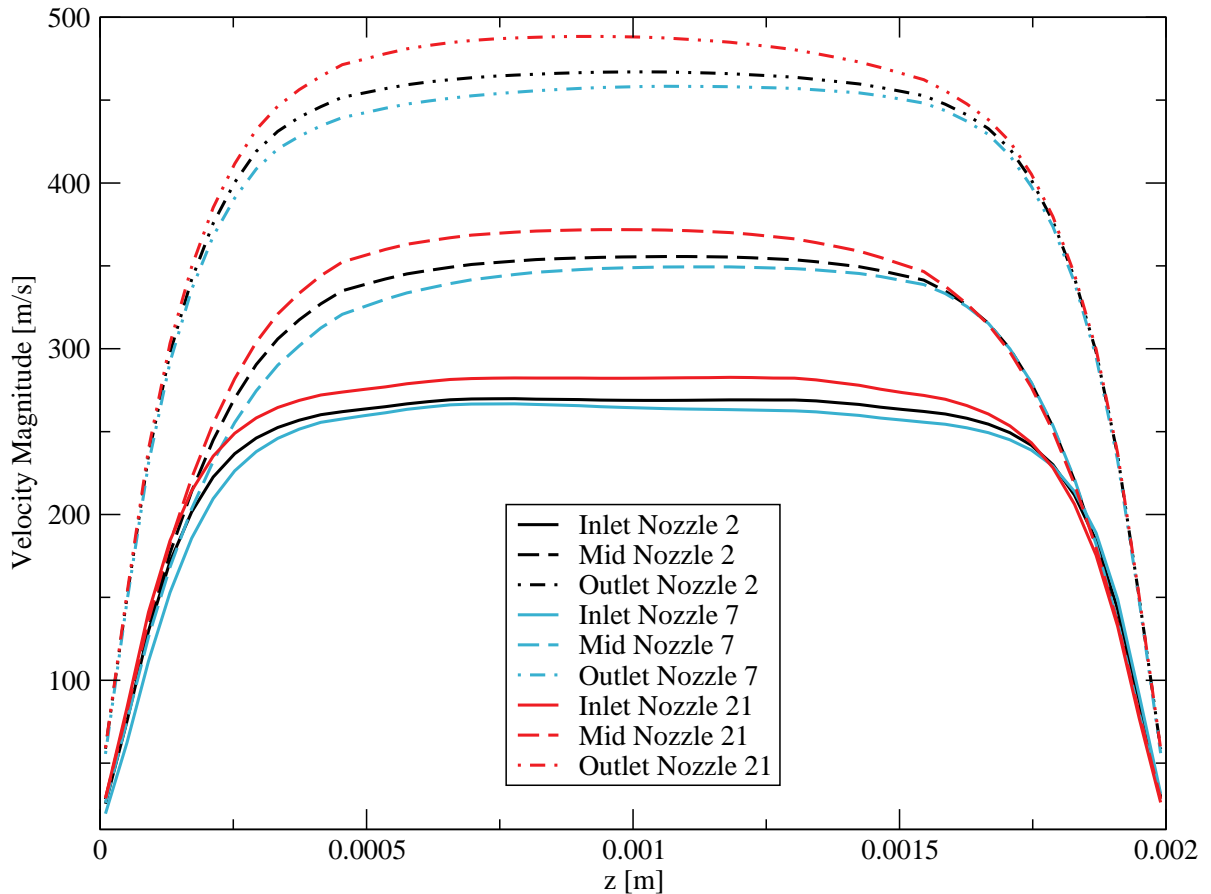
Figure 5.9: Velocity plot for different nozzles and locations.

The thermal and velocity boundary layers of the seventh nozzle which is a critical part of the PVD setup due to the recirculating flow are shown in figure 5.11. From this contour, there is a significant difference between thickness of both boundary layers with the thermal boundary layer a little thicker than the velocity boundary. The ratio of the velocity boundary layer thickness to that of the thermal boundary layer, which is characterised by the Prandtl number, is less than and in agreement with the Prandtl number of gases (Pr = 0.7) [2, 23]. Upon closer inspection, the thermal boundary layer thickness in the upstream side of the nozzle is greater than the downstream side which is due to the disturbed zinc vapour flow leaving the inlet channel. The slightly thicker boundary layer on the upstream side can also be observed in figure 5.12(a). There is no significant difference for the velocity boundary layer looking at the contour, apart from the inlet region. This difference is also seen in the velocity plots along the nozzle boundary layer in figure 5.12(b). Around this inlet region, the velocity upstream is lower since the zinc vapour rushes into the downstream wall of the nozzle as it leaves the inlet channel, therefore causing a thicker velocity boundary layer upstream as compared to downstream in the inlet region.

From the thermal and velocity line plot along the seventh nozzle in figure 5.12, the temperature along the center of the nozzle, midstream, is lower than the temperature close to the wall which is due to the wall heating. The reverse is the case for the velocity plot, because of the no-slip at the walls. For thermal and velocity plots, there is an increase in gradient at the inlet and exit of the nozzle due to the converging and diverging
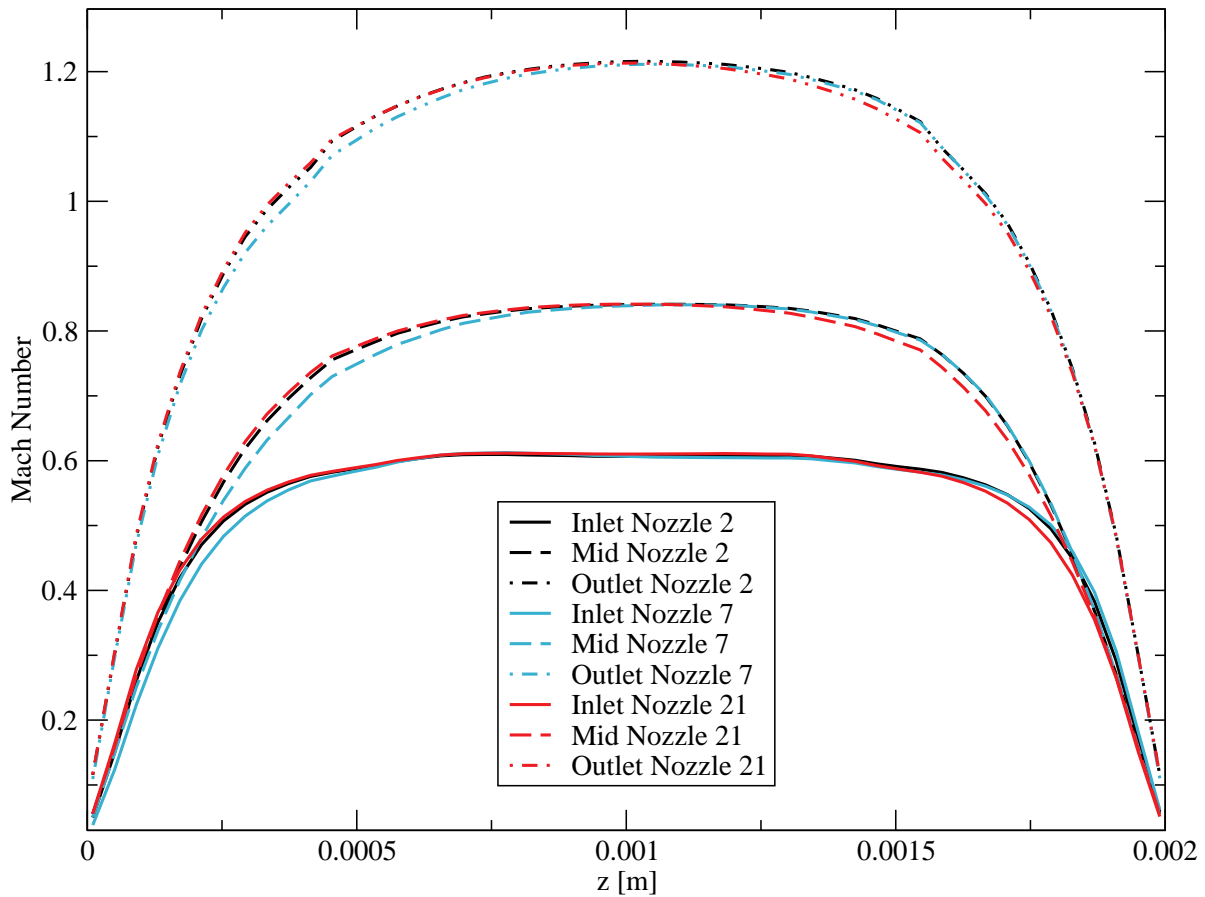
Figure 5.10: Mach plot for different nozzles and locations. The speed of the zinc vapour flow in the nozzles as compared to the speed of sound in this fluid is similar for the different nozzle locations. These profiles are also quite similar to the velocity profiles in figure 5.9.
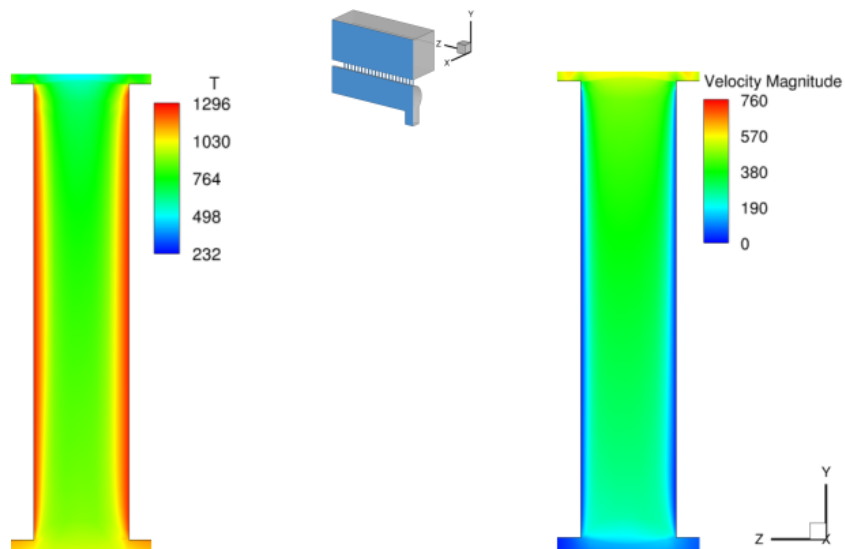
Figure 5.11: Thermal and velocity boundary layers in nozzle seven. There is a thicker thermal boundary layer as compared to the velocity boundary layer, showing the effect of the wall heating and the high speed zinc vapour flow.
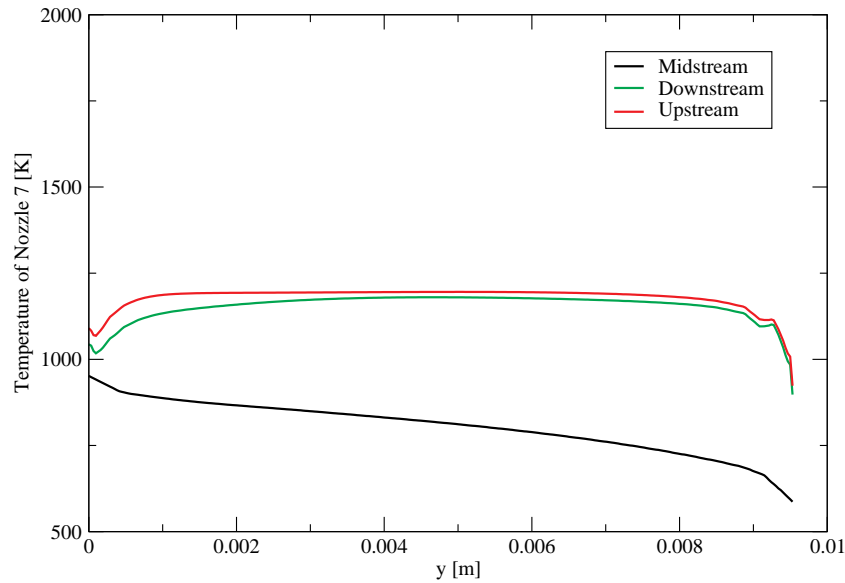
(a) Temperature plots along the nozzle.
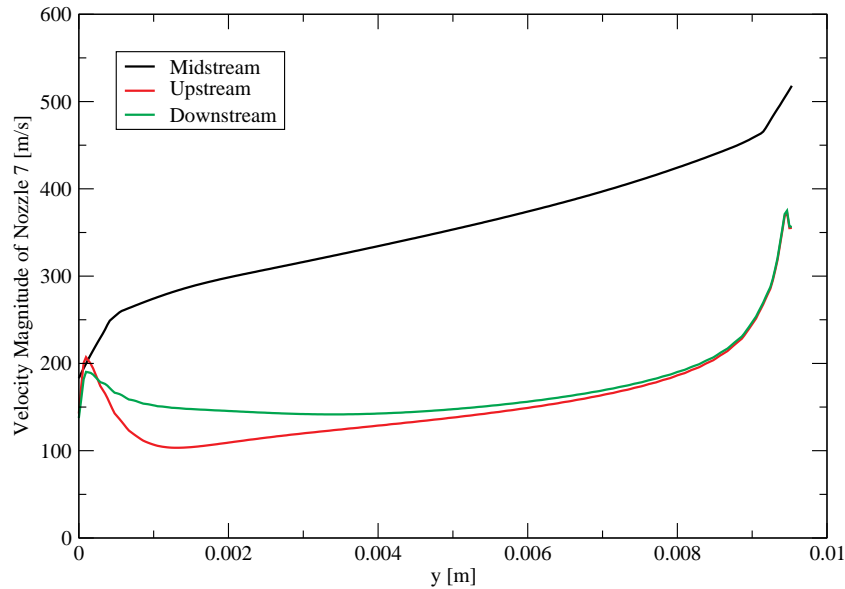
(b) Velocity plots along the nozzle.

Figure 5.12: Temperature and velocity plots along nozzle seven. Sample lines for the plot are shown in figure 5.6. Streamlines crossing these sample lines at the inlet and outlet of the nozzle resulted in the peaks at edges of the plot.

of the zinc vapour flow. Close to the walls of the nozzle, the effect of this converging and diverging zinc vapour flow is more significant as the temperature and velocity gradients around the inlet and exit of the nozzle change sign. The temperature profile between the inlet and outlet of the nozzle close to the wall is constant due to the constant wall heating, but the temperature midstream drops as the zinc vapour flows from the inlet to exit of the nozzle. This drop in temperature is due to the decrease of pressure within the nozzle that speeds up the zinc vapour flow. For the velocity plot, there is speed up for all streams, with the flow through the center having the greatest speed up since it is farthest from the wall.
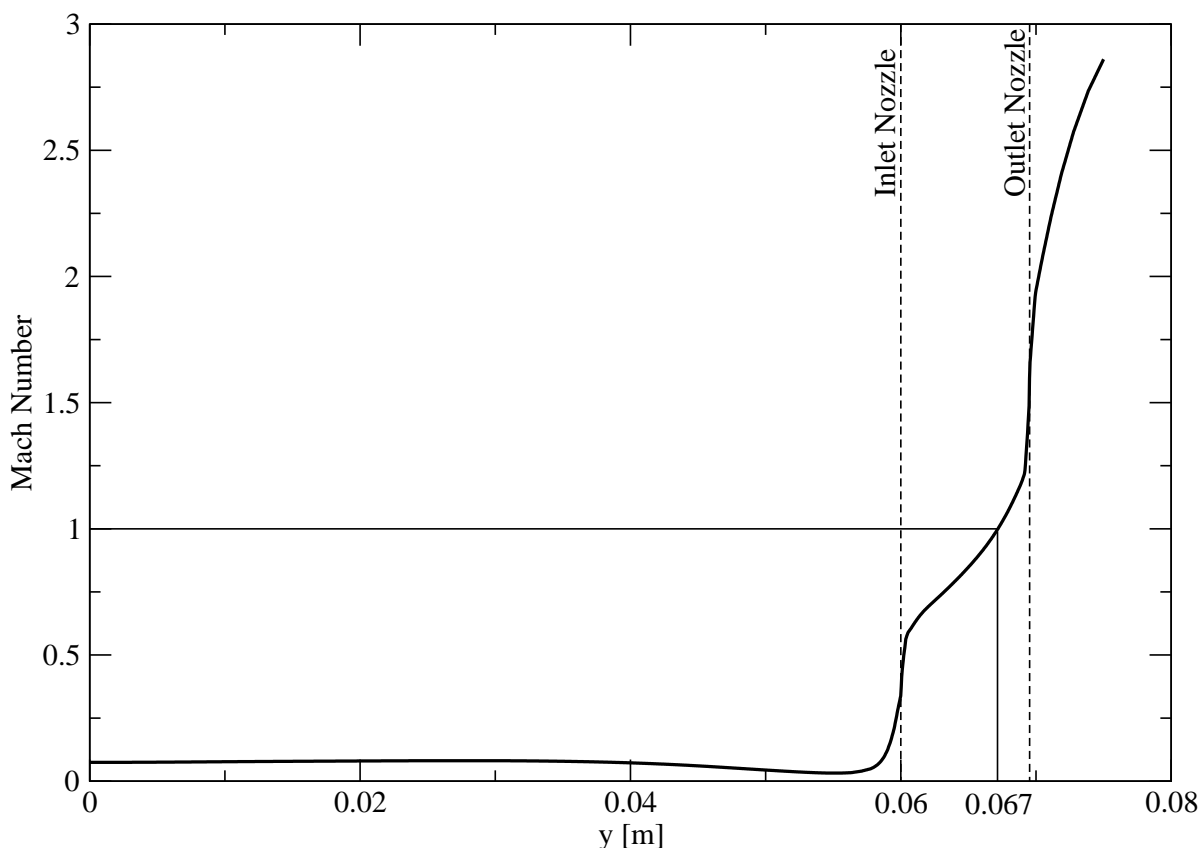
Figure 5.13: Mach number plot going through the center of the VDB. The nozzle region and the position in the nozzle where the flow is choked can be seen.

Figure 5.13 shows the plot of the Mach number through the center of the VDB past the central nozzle. From this plot, moving along the center of the VDB, the flow can be described as incompressible since the Mach number is less than 0.3 [5, 19]. There is a sharp gradient before entering the nozzles at the inlet and exit of the nozzle where the Mach number increases rapidly due to the converging and diverging zinc vapour flow. The flow chokes after the midway through the nozzle. As the flow exits the nozzle, the supersonic Mach number is reached.

In figure 5.14, drop in pressure resulted in increased recirculation zone which adversely affects the symmetrical flow in the nozzle, but with lower background pressure the nozzle effect reduces due to the high pressure gradient across the nozzles in figure 5.15. Furthermore, this high recirculation zones increases the heat zone in the VDB which would lead to lower tendency of condensation in the VDB channel.

5.2. Mass Flow Rate Analysis from Nozzles

From mass conservation, the mass flow rate through a channel is constant for a steady state flow and depends on the density, velocity and area of the channel. Increasing the mass flow rate of an incompressible flow is as simple as increasing the velocity of the flow. This is not the case for real fluids since compressibility influences how much of the flow speed can be increased. The mass flow rate of the compressible zinc vapour flow through the nozzles of the PVD set-up thus depends on the state of the gas, properties
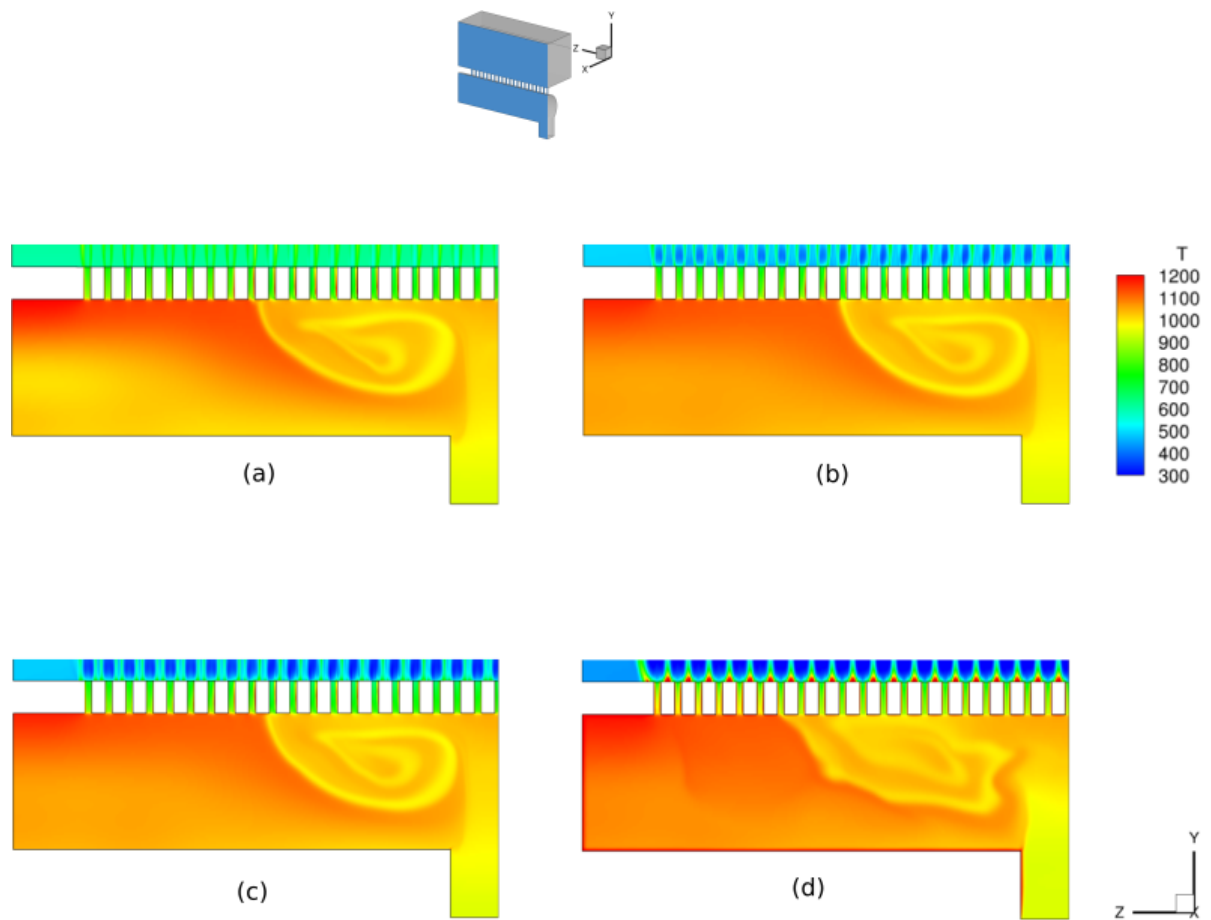
Figure 5.14: Temperature field for varying conditions. (a) Case 1. (b) Case 2. (c) Case 3. (d) Case 4

of the zinc vapour and Mach number. This mass flow rate,

$$\dot{m} = p_t \sqrt{\frac{\gamma}{RT_t}} \mathrm{M}A\left(1 + \frac{\gamma-1}{2}\mathrm{M}^2\right)^{-\frac{\gamma+1}{2(1-\gamma)}} \tag{5.1}$$

of a compressible gas is derived using the stagnation pressure and temperature equations similar to (2.14), where the subscript t means total. p_t is the summation of the static and dynamic pressure at a particular point in the flow, T_t is the temperature at that location, A is the cross-section of the nozzle/channel, M is the Mach number as described in (2.2), γ is the specific heat ratio in (2.4), and R is zinc gas constant. The maximum achievable mass flow rate occurs when the flow is choked and thus (5.1) reduces to,

$$\dot{m} = p_t A^* \sqrt{\frac{\gamma}{RT_t}}\left(\frac{\gamma+1}{2}\right)^{-\frac{\gamma+1}{2(1-\gamma)}} \tag{5.2}$$

and A^* is the critical area of the nozzle where the flow is choked [18, 28]. But since the nozzle of the current PVD set-up is cylindrical, the critical area remains the same as the area in (5.1). Therefore, from (5.1) and (5.2), to increase the mass flow rate we can either increase the area and the total pressure or decrease the total temperature.

For the PVD process, the mass flow rate at the exit of the individual nozzles is computed by integrating the flow from the cell faces at the nozzle exit. The resulting mass flow rate is shown in figure 5.16. However, using the isentropic expression in
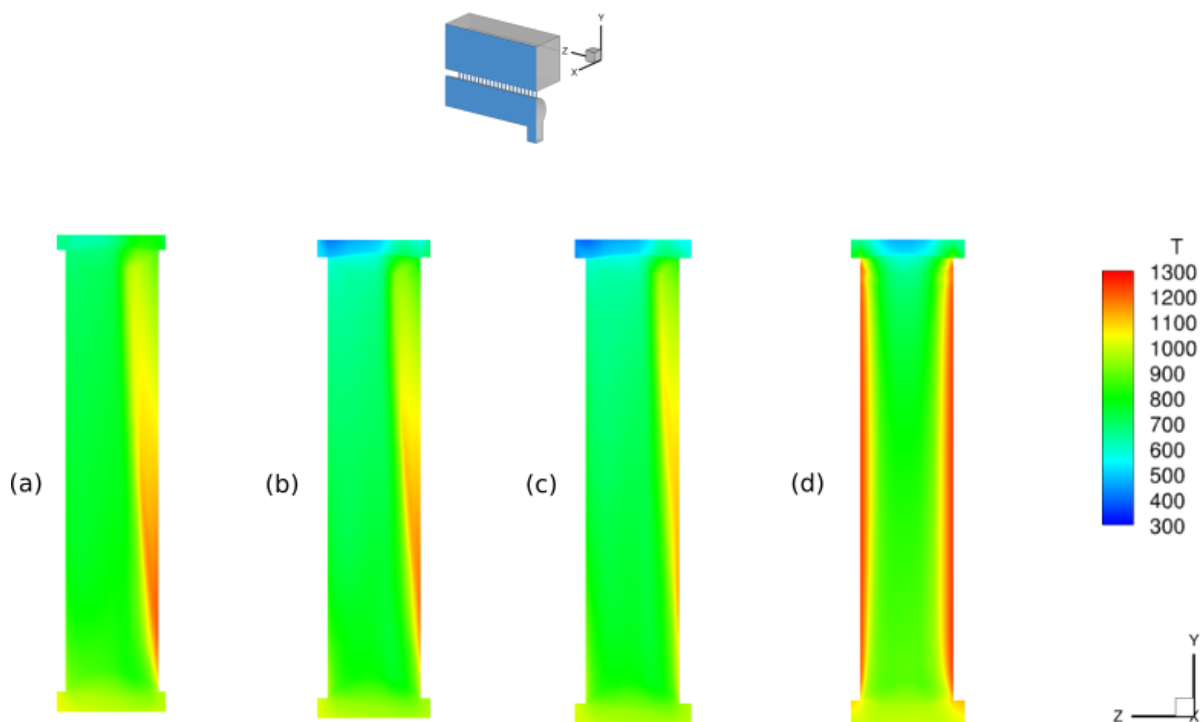
Figure 5.15: 7th nozzle temperature field for varying conditions. (a) Case 1. (b) Case 2. (c) Case 3. (d) Case 4

(5.2), a mass flow rate of $7.88x10^{-5}$kg/s was computed. This value is approximately fives times higher than the average simulated value of $1.6x10^{-5}$kg/s from a nozzle.

From the figure, the nozzles affected by recirculation have the largest mass flow rates as compared to the nozzles at the end of the lateral VDB channel. This difference arises from the increased stagnation pressure in the nozzles close to the inlet channel due to the impact of the swirling flow around the corner of the inlet channel. There is a decreasing trend for the nozzles at the end of the lateral channel of the VDB that should be taken note of, because this drop in mass flow rate would increase for a longer channel when the VDB is scaled up. And this would increase the difference in mass flow from the nozzles in the recirculation region with the nozzles at the tail end of the channel, leading to an even more non-uniform deposition of zinc. For the present setup at Tata steel in figure 5.16, the difference in mass flow rate leads to a 5.05% difference in thickness of the deposited zinc. This difference which would not lead to a poorly protected steel surface since the zinc acts as a sacrificial anode where the corrosion takes place instead of the steel plate. According to Tata steel standards [39], a zinc surface finish from hot deep galvanizing (HDG) which has five times the thickness in zinc layer of the physical vapour deposition of zinc has a roughness limit of 1.4μm. The maximum difference in mass flow rate results in deposition difference which is three orders of magnitude less than this standard value from HDG. Thus, with regards to surface roughness, the non-uniformity in zinc deposition is acceptable.

From figure 5.16, it can be concluded that the last six nozzles of the VDB leads to a relatively poor appearance. These nozzles can be closed by Tata steel, and further experiments can be carried out to observe if the surface finish still appears non-uniform. The mass flow rate for inviscid cases decreases with decreasing outlet pressure in figure
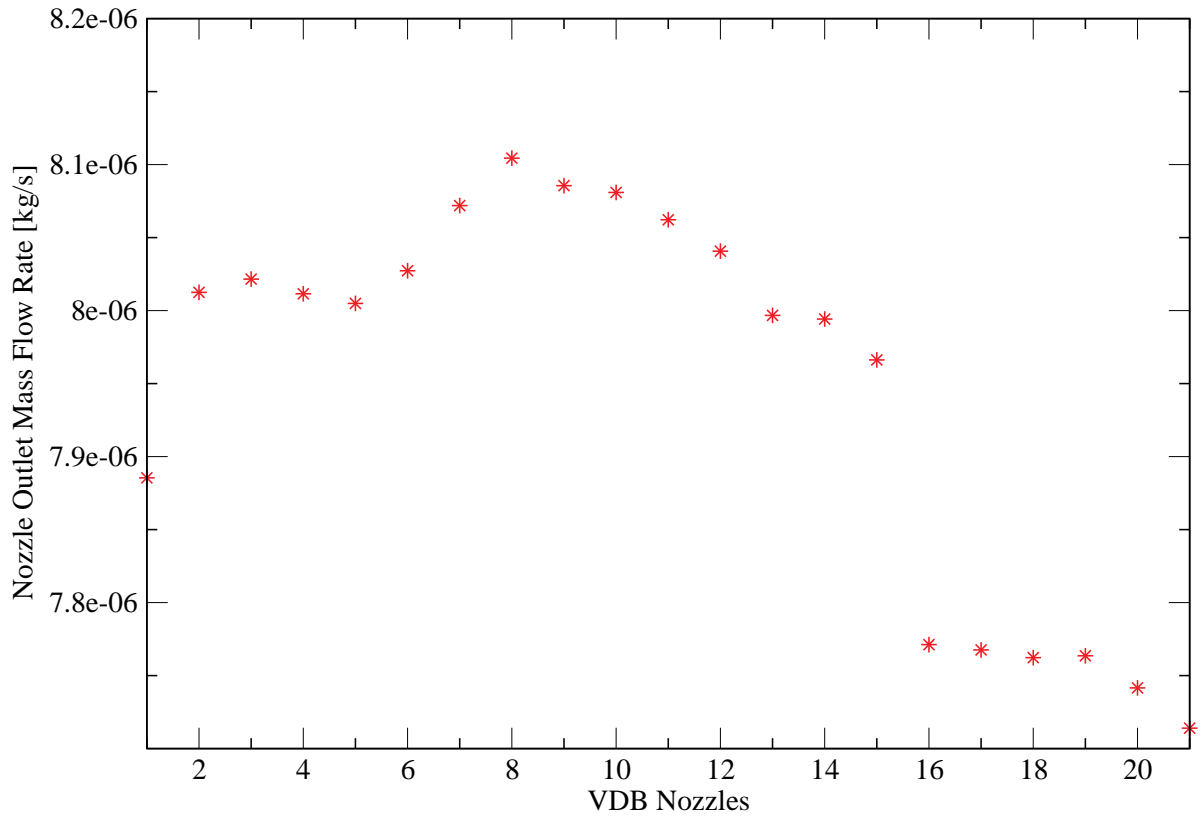
Figure 5.16: VDB nozzle mass flow rate. The quarter geometry mass flow rate is considered. The mass flow rate of the first nozzle is multiplied by two due to the double symmetry. Refer to figure 5.6 for the nozzle numbering.

5.17, which is not expected since higher pressure gradient should result in high mass flow rate. However, for the viscid case, there is no difference in mass flow rate for 1 Pa and 0.01 Pa.

5.2.1. PVD Process Validation

To check the fundamental physics of the CFD simulation, values from the simulation are compared with experiments. But as discussed in the introduction, we are limited to what we can compare due to the data collected from Tata steel. From Tata steel, the zinc vapour is deposited on a 30cm steel strip moving with a speed of 2m/min and a zinc layer of $1.8 - 2\mu$m is formed on the steel strip. The resulting mass flow rate from this data is 1.43×10^{-4}kg/s. And integrating the mass flow rate over all the nozzle exit areas of a full VDB for the CFD simulation yielded 6.52×10^{-4}kg/s. The difference in mass flow rate could be attributed to various experimental losses due to stray deposition on the walls of the vacuum chamber, some errors could be attributed to the numerical schemes and discretization error, inadequate temperature measurement, inaccuracies in the inlet boundary condition. However, it can be concluded that the CFD simulation gives an approximation in the same order of magnitude as the experimental process at Tata steel.

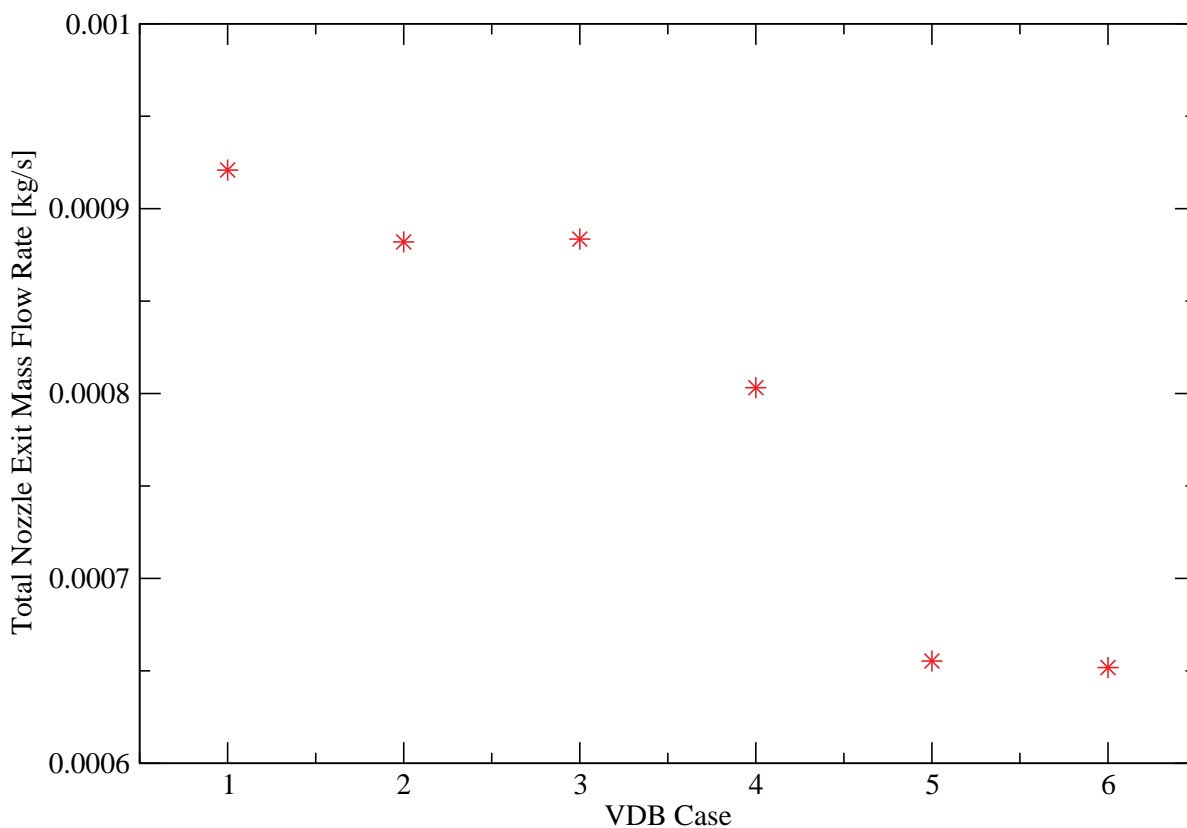Figure 5.17: Variation in nozzle exit mass flow rate for different VDB cases. For the different cases, the complete geometry mass flow is considered.

5.3. Condensation in the VDB and Nozzles

Clusters of zinc atoms are seen on the steel strip after the deposition process is complete. These zinc drops are either from the zinc melt, formed inside the VDB and nozzles, or after the zinc vapour has left the nozzles and collides in vacuum before landing on the steel plate. Since this thesis focuses on the VDB and nozzles, the possibility of droplet formation in these regions depend on the position in the vapour phase diagram but also on the collision of the zinc atoms. To carry out the analysis for the vapour pressure diagram, the vapour pressure distribution in the VDB and nozzles has to be determined. This is done using the Antoine equation from Smithells metals book[7],

$$\log p = -\frac{A}{T} + B + C\log T + 10^{-3}DT \tag{5.3}$$

where p is the vapour pressure in mmHg, T is the temperature in the VDB and nozzles, and A, B, C and D are constant Antoine coefficients [41]. The Antoine coefficients for the working temperature ranges are shown in table 5.1. The resulting vapour pressure of the PVD process is shown in figure 5.18. However, since the Antoine coefficients starts around 473K, the temperature in the expansion box of the set-up - after the nozzle - is not captured. Thus, consideration is only given to the VDB and nozzles.

After the vapour pressure of the VDB and nozzles are computed, the pressure in the set-up is compared to the vapour pressure values with the resulting contour in figure 5.19. From figure 5.19, apart from a region close to the inlet and the nozzles, all other

Table 5.1: Antoine coefficients for temperature ranges of zinc.

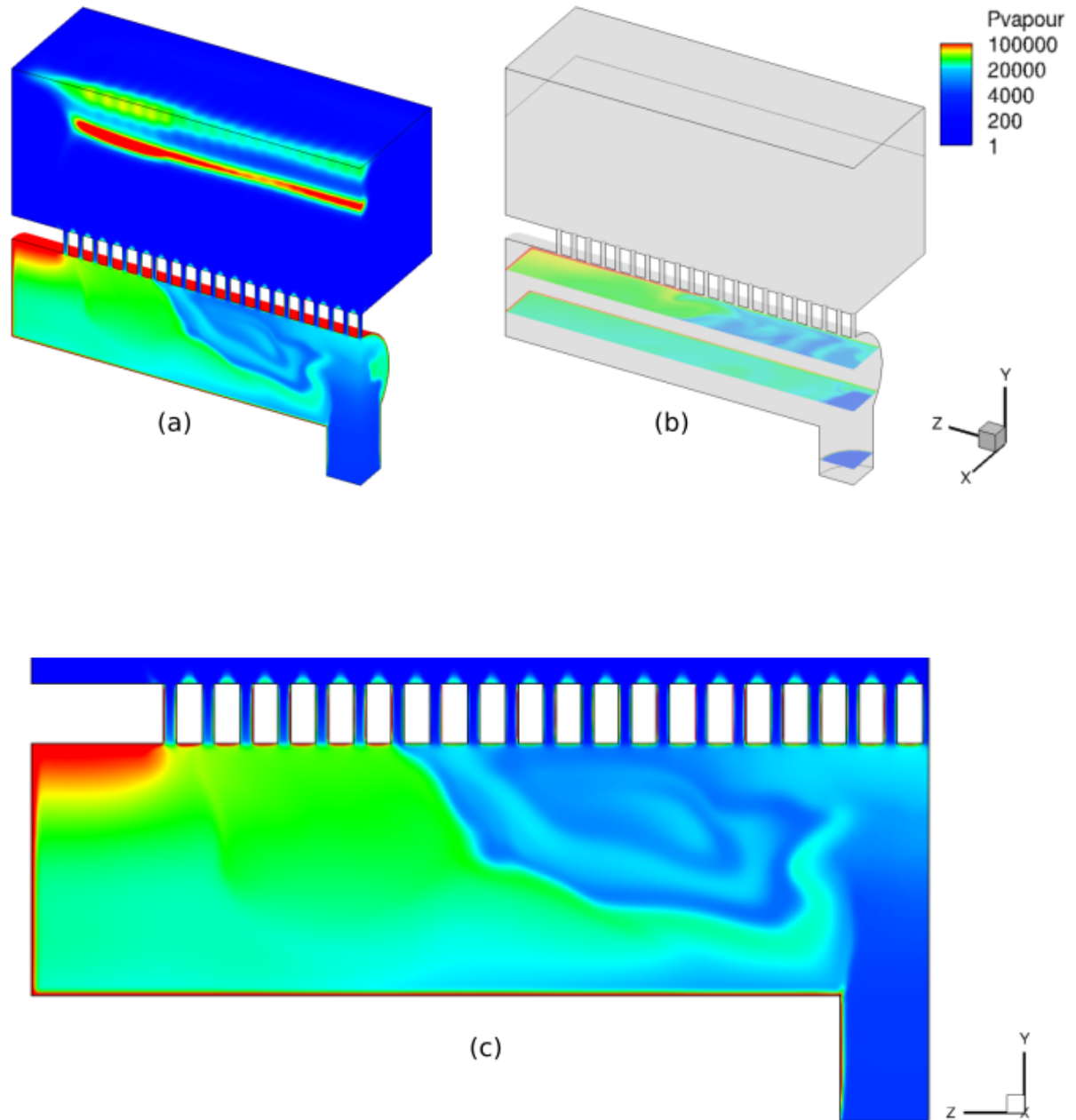| Antoine coefficients	Temp. range: 473 - 692.5 K	Temp. range: 692.5 - 1000 K
A	6883.0	6670.0
B	9.418	12.0
C	-0.0503	-1.126
D	-0.33	0

Figure 5.18: Saturation pressure contour using the Antoine coefficients. (a) Three dimensional contour of the VDB and nozzles. (b) x-z contour planes in the VDB. (c) y-z plane of the vapour pressure contour with focus on the circulation region similar to the temperature contour in figure 5.2 (b).

regions have no likelihood to form zinc droplets as shown on the x-z planes in figure

5.19(b). Thus a droplet can be formed close to the inlet and flow out through the nozzles which are all above the vapour pressure. Zinc vapour can also form droplets before leaving the nozzles because they are all above the vapour pressure. Observing figure 5.19(c) carefully, the nozzles at the end of the lateral VDB channel have lower regions above the vapour pressure and thus are less likely to form droplets. More investigations shows that the nozzles affected by recirculation are most likely to produce droplets since they have almost all regions of the nozzle above the vapour pressure. Other studies showed that increasing the diameter of the nozzles and the number density or pressure, while decreasing the temperature would lead to cluster formation and growth of metal droplets, since the above conditions increases the the tendencies of zinc atom collision [15, 16]. Reducing the length of the nozzles could however decrease the likelihood of the zinc vapour clustering since the region of droplet formation is decreased.
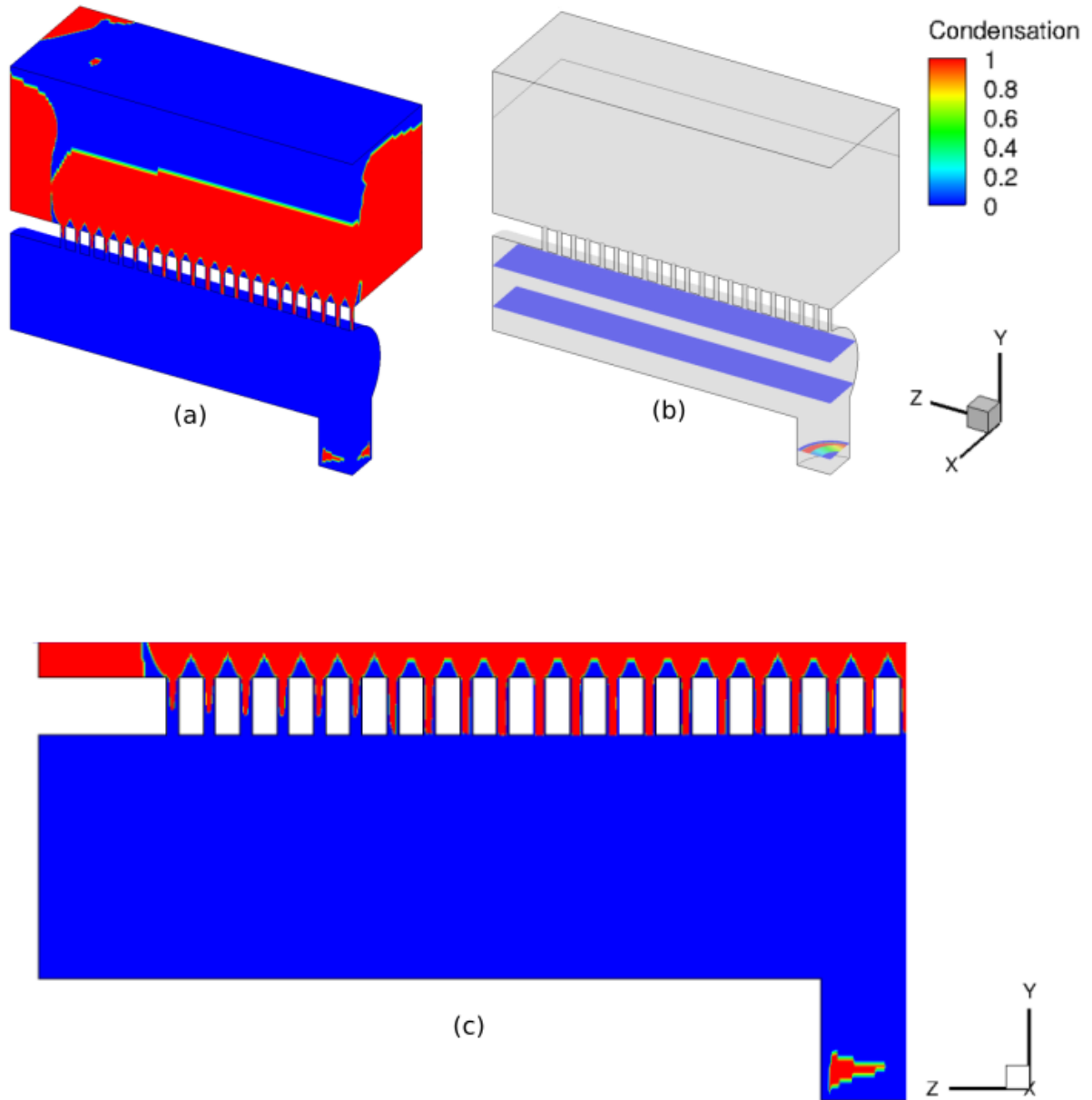
Figure 5.19: Condensation contour showing the likelihood of the zinc vapour forming droplets as 1 and 0 otherwise. (a) Three dimensional contour of the VDB and nozzles. (b) x-z contour planes in the VDB. (c) y-z plane of the condensation contour with focus on the nozzles.

6

Conclusions and Recommendations

Numerical simulations of the zinc vapour flow, heat and mass transfer for the PVD process at Tata Steel have been performed for viscid and inviscid cases with varying background pressure. From this research thesis, the following conclusions are reached:

The small nozzle outlet area resulted in a uniformly built up pressure in the VDB, which is necessary for uniform deposition from the nozzles. A recirculation could be observed next to the inlet stream from the streamlines and temperature. The recirculation pattern observed in the temperature in the VDB is stable and influences both the mass flow rate and condensation likelihood in the nozzles.

The mass flow rate from the simulation gave a good first approximation but overpredicted the experimental value by a factor four, possibly due to stray deposition, inadequate inlet temperature measurement and numerical errors. The isentropic mass flow rate equation (5.2) gave a five times higher mass flow rate than the simulation, reasons could be the heating of the VDB wall and viscous effects especially close to the nozzle wall, which decrease the critical area. The mass flow rate from the nozzles at the end of the VDB, behind the recirculation region, is smaller, which can affect uniformity after scale up.

For the lowest outlet pressure, the effect of recirculation on the nozzle flow becomes reduced leading to more symmetrical flow, while higher outlet pressures resulted in huge difference in upstream and downstream field variables. The mass flow rate decreases for decreasing outlet pressure for inviscid cases (which was not expected). The mass flow rate for the viscid case is less than inviscid due to the thicker velocity boundary layer from fluid friction. Although there is a general drop in mass flow rate as the background pressure decreases, there is no significant difference in the nozzle exit mass flow rate for a viscid case with outlet pressure of 1 and 0.01 Pa respectively.

Condensation within the VDB is most likely to occur in the nozzles based on the Antoine equation. However, formation of zinc droplets is less likely in the nozzles far away from the inlet channel. Short nozzles give probably a similar mass flow (as it is expected to choke in the nozzles due to the high pressure gradient), but a smaller region where condensation is likely [4].

Recommendations

Based on the research goals and the plans of Tata Steel for the PVD process, the following recommendations are given:

To increase the mass flow rate, a parametric study can be carried out on the melt temperature and corresponding inlet vapour pressure on how this affects the deposition rate and the vapour pressure as a result of condensation. Tata Steel intends to scale-up the process requiring a fifty times higher mass flow rate, which is not achievable with an increase in melt temperature alone, different nozzle configurations should be designed, like the diverging nozzle in order to carry out computational studies to achieve higher mass flow rate.

Simulations with varying the nozzle length should be carried out to confirm the reduction in condensation regions predicted by Bayazitoglu et al. [4]. The mesh used to carry out the simulation was able to resolve the velocity gradient at the nozzle boundary for a viscid case but not for an inviscid case with sharper velocity boundary gradient. Thus, the mesh in the nozzles can be more refined for more accurate results depending on the simulation to be performed. However, care should be taken around meshing the converging and diverging regions since they have high tendencies to be non-orthogonal as the nozzle mesh becomes more refined.

Before the above mentioned physics can be studied, the deviation between the simulated and experimental mass flow rate has to be addressed. Firstly, the sensitivity of the mass flow rate with respect to the melt temperature should be studied. Another reason for the deviation could be the assumption of a zero gradient inlet velocity boundary condition, possibly overpredicting the inlet flow velocity. Further improvements would be to include turbulence modelling since there is larger space for turbulent eddies to develop and high shear stresses at the boundary of the inlet stream. Simulations should be performed with fluctuations added at the inlet boundary condition. For this study, a pressure based solver was used, however, for future work density based solvers (such as dbnsFoam, which was tested in the appendix D) should be investigated in order to achieve a better prediction in the nozzle. A combination of the pressure and density based solver can also be attempted to obtain a more accurate balance between stability and accuracy.

A

Mesh Study

The plots in figure A.1 show the temperature contours of an inviscid case with 1000 Pa outlet pressure of different mesh sizes. As can be seen from the contours of the different mesh sizes, the effect of recirculation which also leads to a boundary layer on the upwind wall of the nozzle of 0.75 million cells could not capture this phenomenon properly.
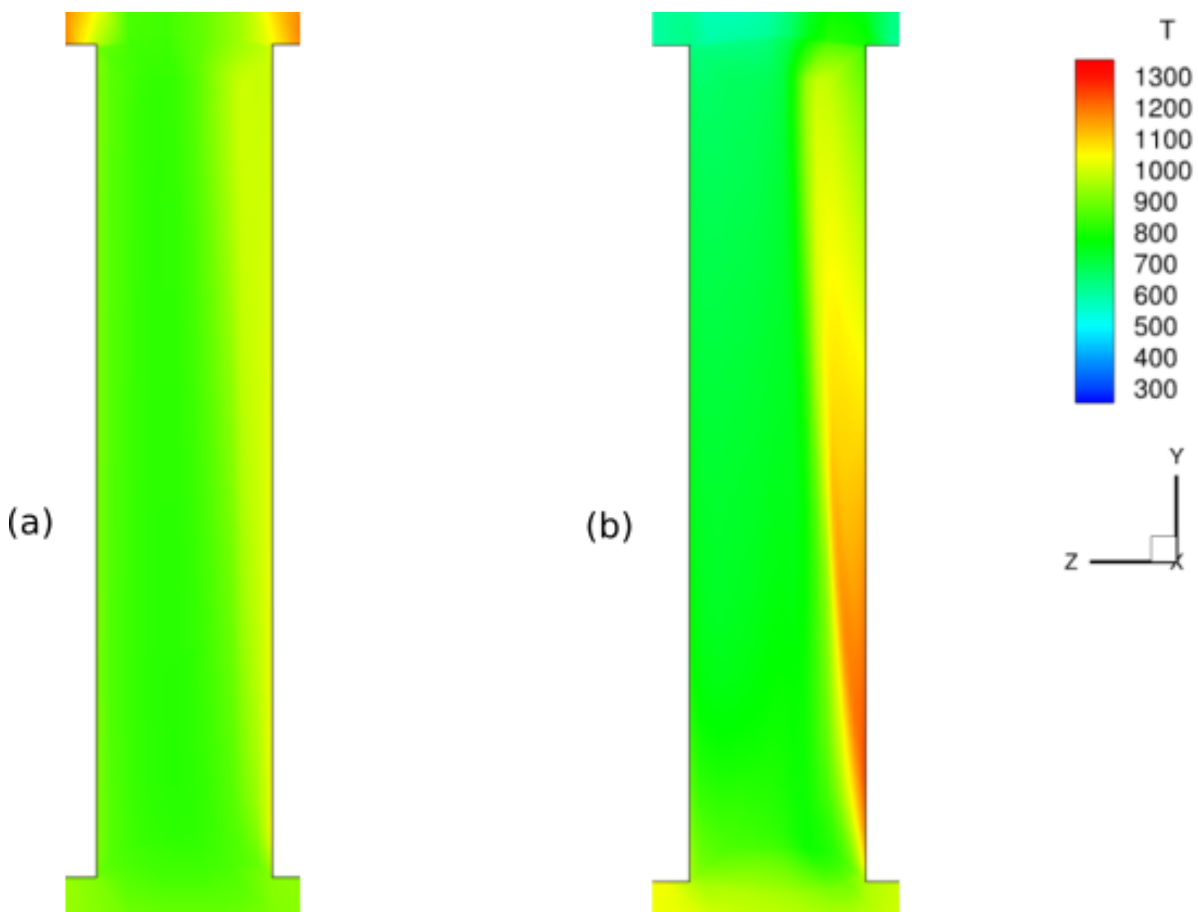

Figure A.1: y-z plane temperature plot of the seventh nozzle. (a)Mesh of 0.75 million cells (b)Mesh of 2.3 million cells.
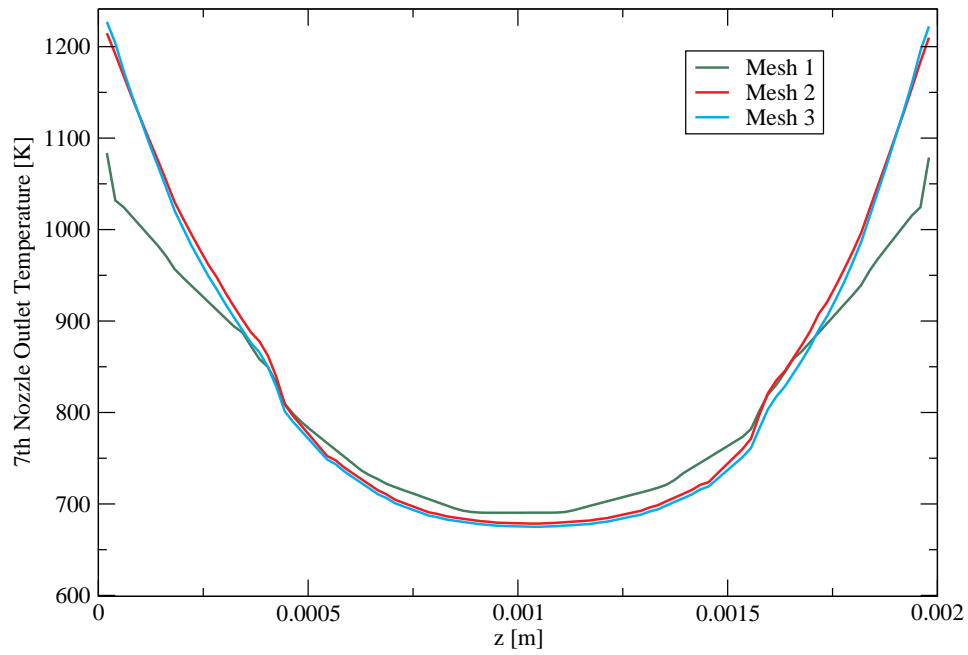
Figure A.2: 7th nozzle temperature profile for VDB case 4. Mesh 2 gives a close approximation to the mesh 3, and requires less than half the computation time. Mesh 1 does not properly resolve the temperature gradient close to the wall.

Figure A.3: 7th nozzle Mach number profile for VDB case 4. The mesh 2 viscid plot is case 6 and can be see to largely vary from the inviscid case 4 due to less steep velocity gradient close to the nozzle wall leading to a more resolved velocity boundary field.

B

Convergence

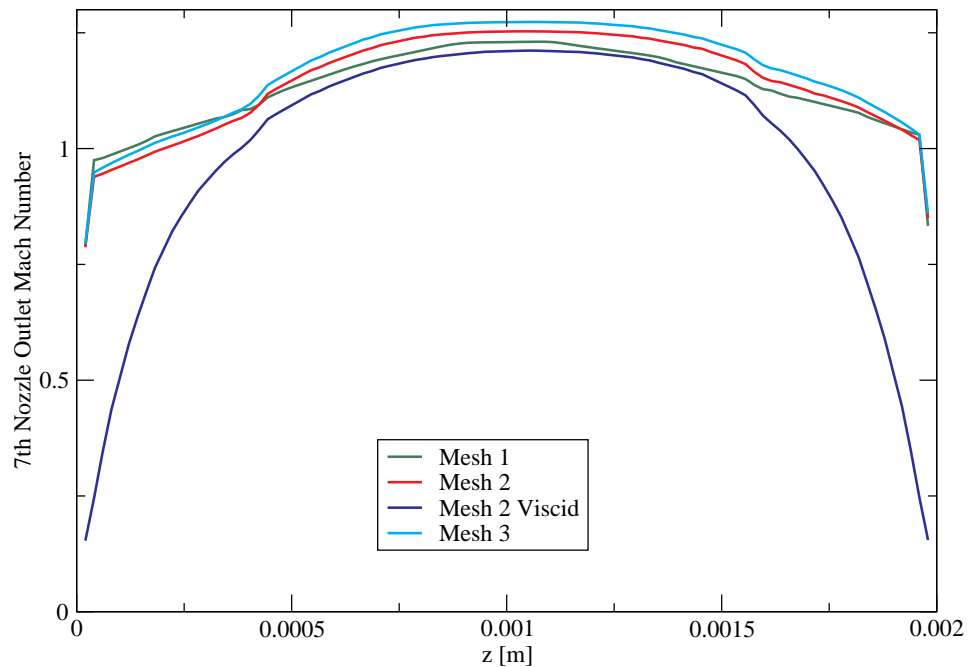To justify the simulation does not change in time, a temperature plot at an instance in time and a plot averaged over time in figure B.1. From the plot, the recirculation around the corner of the inlet channel and other phenomena can be observed in both figures, thus suggesting T = Tmean which implies a steady state is reached.
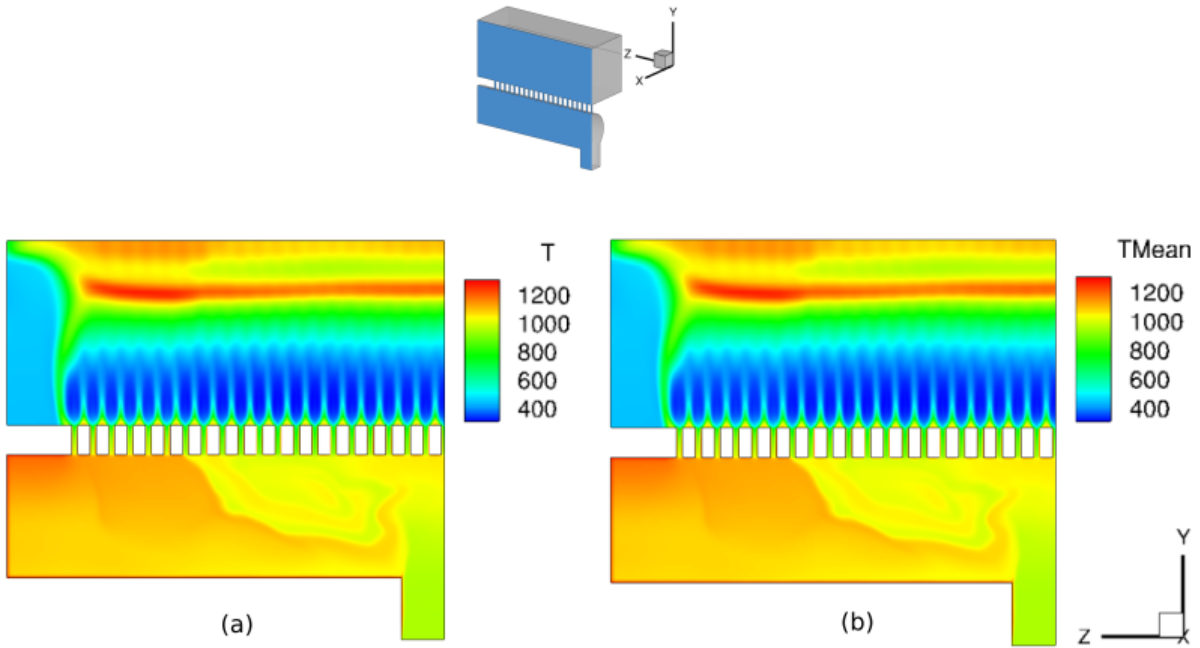
Figure B.1: y-z plane temperature contour of VDB case 6. (a) At an instance in time (b) Averaged over 850,000 iterations in 0.0117 s.

To quantitatively understand the level of fluctuation in the VDB and nozzles, U_{rms} contour was computed and seen in figure B.2. The root mean square velocity is related to the velocity fluctuations as follows,

$$U_{rms} = \sqrt{\frac{1}{3}(u_x'^2 + u_y'^2 + u_z'^2)}, \tag{B.1}$$

where the fluctuations are $u_i' = u_i - \bar{u}$ [30], and $\bar{u}$ is the averaged velocity. From the U_{rms} contour in figure B.2, the maximum deviation from the mean velocity in the VDB

and nozzles is around 2.5 m/s in most regions of the VDB. Thus, the VDB and nozzle can be assumed to be quasi-steady. However, although the averaged field variables and instantaneous variables are the same, there are relatively high turbulent intensity in the VDB which should be further investigated.
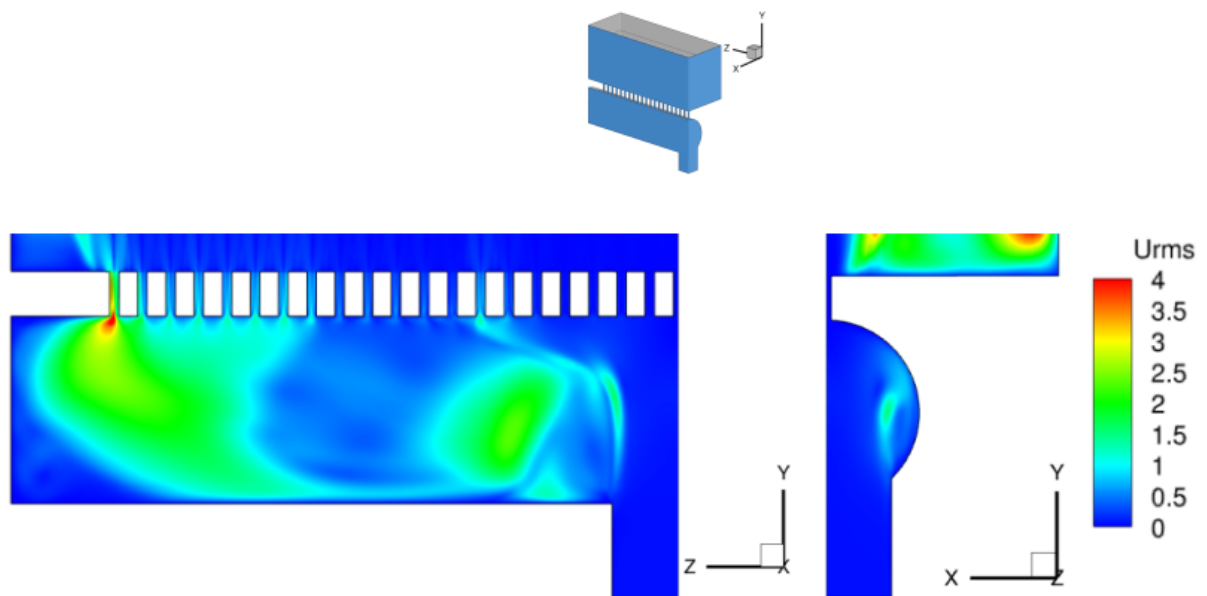
Figure B.2: Root mean square velocity (m/s) contour of VDB case 6.
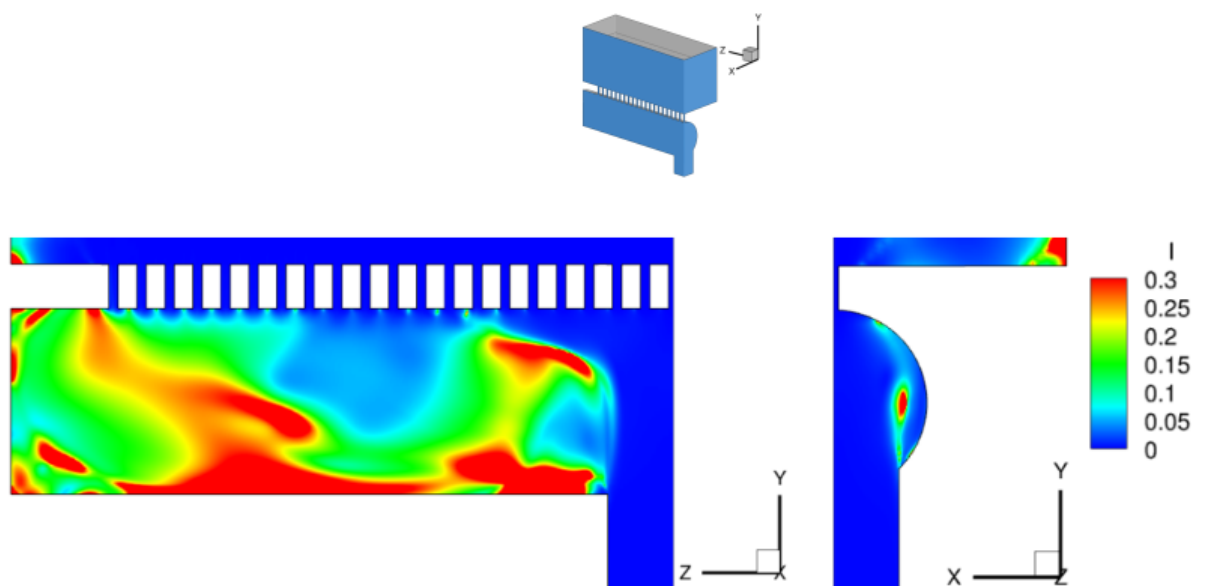
Figure B.3: Turbulent Intensity contour of VDB case 6.

B.1. Mass Flow Rate Convergence for Varying Cases

The plots below show the VDB convergence for different conditions. And all plots can be observed to reach steady state as required for the post-processing of result.

(a) Case 1

(b) Case 2

(c) Case 3

(d) Case 4

(e) Case 5

(f) Case 6
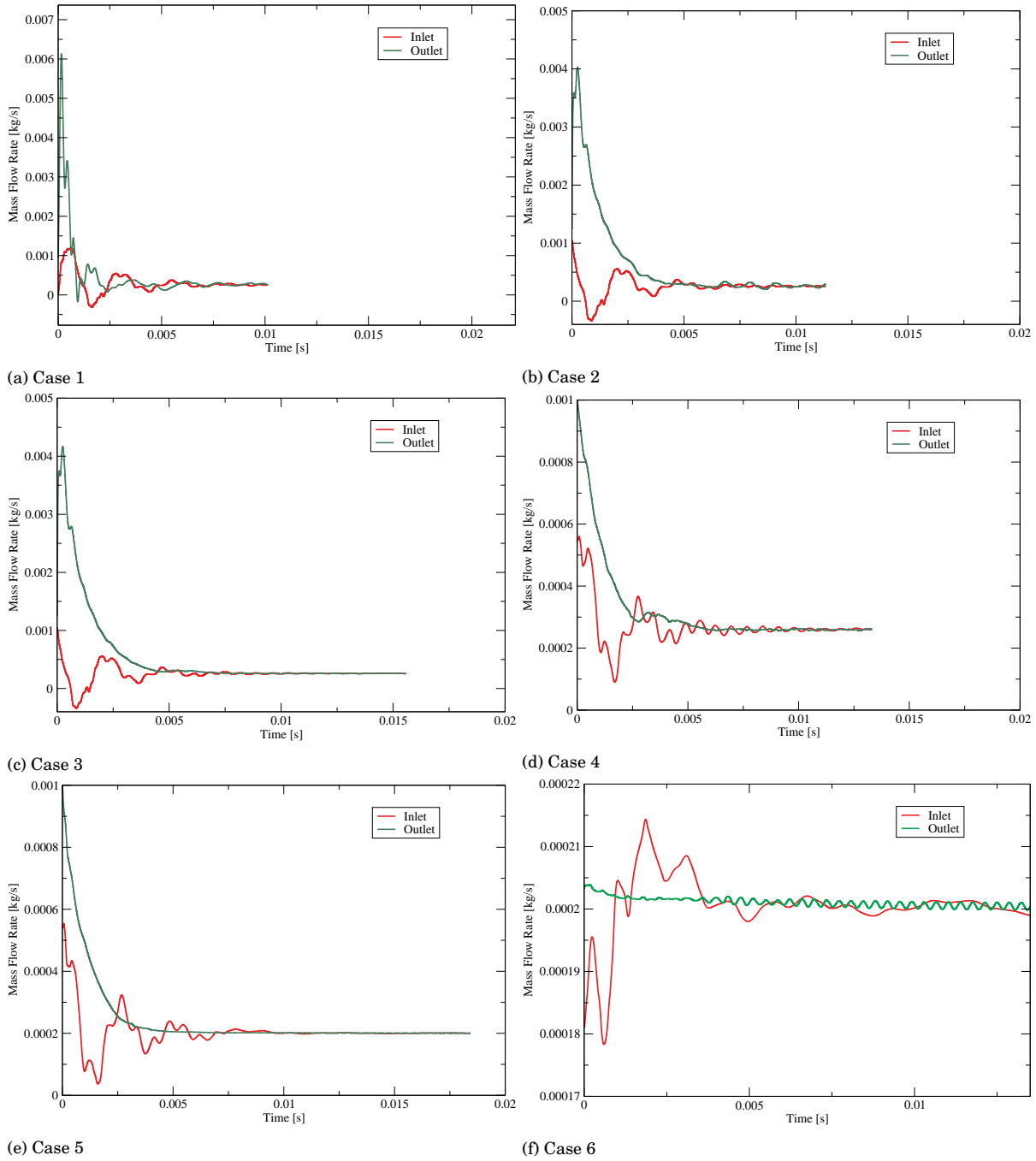
Figure B.4: VDB Mass Flow Rate Convergence for Varying Conditions.

C

Vapour Pressure and Condensation Functions

The following Tecplot macro is used to compute the vapour pressure and the probability of condensation in the VDB and nozzles.

```
#!MC 1410
$!ALTERDATA
  EQUATION = '{mmHgToPa}=133.322368'
$!ALTERDATA
  EQUATION = '{A1}=6883.0'
$!ALTERDATA
  EQUATION = '{B1}=9.418'
$!ALTERDATA
  EQUATION = '{C1}=-0.0503'
$!ALTERDATA
  EQUATION = '{D1}=-0.33'
$!ALTERDATA
  EQUATION = '{A2}=6670.0'
$!ALTERDATA
  EQUATION = '{B2}=12.0'
$!ALTERDATA
  EQUATION = '{C2}=-1.126'
$!ALTERDATA
  EQUATION = '{D2}=0'
$!ALTERDATA
  EQUATION = '{Pvapour1}=-{A1}/{T}+{B1}+{C1}*LOG10({T})+0.001*{D1}*{T}'
$!ALTERDATA
  EQUATION = '{Pvapour1}={mmhgToPa}*10**{Pvapour1}'
$!ALTERDATA
  EQUATION = '{Pvapour2}=-{A2}/{T}+{B2}+{C2}*LOG10({T})+0.001*{D2}*{T}'
$!ALTERDATA
  EQUATION = '{Pvapour2}={mmhgToPa}*10**{Pvapour2}'
$!ALTERDATA
  EQUATION = '{Pvapour}=IF({T}<=692.5,{Pvapour1},{Pvapour2})'
$!ALTERDATA
```

```
  EQUATION = '{rho}={p}/(127.2*{T})'
$!ALTERDATA
  EQUATION = '{Ptotal}={p}+(0.5*{rho}*{VelocityMagnitude}**2)'
$!ALTERDATA
  EQUATION = '{Condensation}=IF({Ptotal}<{Pvapour},0,1)'
```

D

Density Based Solver
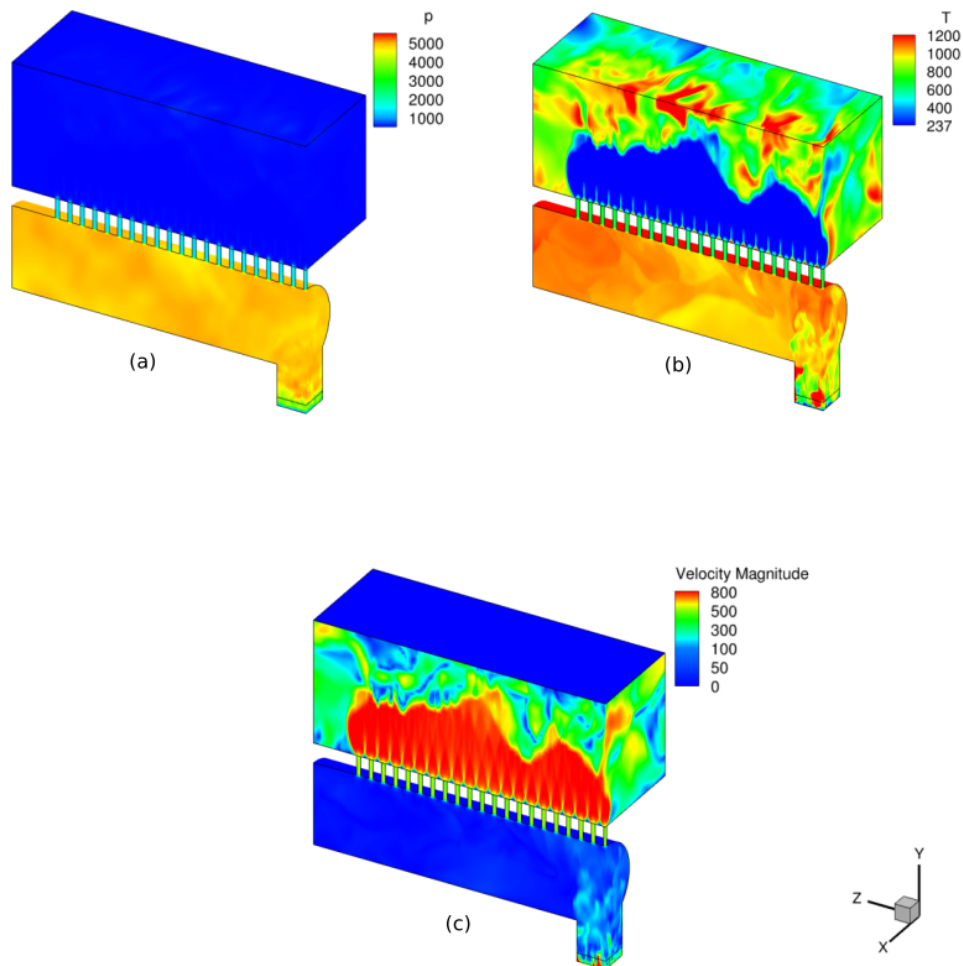
Figure D.1: Inviscid PVD simulation contour using dbnsFoam for 0.01 Pa outlet pressure. (a) Pressure in Pa. (b) Temperature in K. (c) Velocity magnitude in m/s. Further investigation of the inlet conditions should be carried out due to the over estimation of the field variables at the inlet region. The mass flow rate of 2.51×10^{-4}kg/s for this quarter VDB after averaging over the exit nozzle as compared to the pressure based with the same conditions of 2.01×10^{-4}kg/s.

49

Bibliography

[1] SMA Noori Rahim Abadi, A Ahmadpour, SMNR Abadi, and Josua P Meyer. Cfd-based shape optimization of steam turbine blade cascade in transonic two phase flows. *Applied Thermal Engineering*, 112:1575–1589, 2017.

[2] Pierre Andries, Patrick Le Tallec, Jean-Philippe Perlat, and Benoıt Perthame. The gaussian-bgk model of boltzmann equation with small prandtl number. *European Journal of Mechanics-B/Fluids*, 19(6):813–830, 2000.

[3] ICEM ANSYS. Cfd tutorial manual, release 14.5, accessed on 30 october 2012.

[4] Y Bayazitoglu, FR Brotzen, and Y Zhang. Metal vapor condensation in a converging nozzle. *Nanostructured materials*, 7(7):789–803, 1996.

[5] Hester Bijl and Pieter Wesseling. A unified method for computing incompressible and compressible flows in boundary-fitted coordinates. *Journal of Computational Physics*, 141(2):153–173, 1998.

[6] Graeme A Bird and JM Brady. *Molecular gas dynamics and the direct simulation of gas flows*, volume 5. Clarendon press Oxford, 1994.

[7] Eric Adolph Brandes and GB Brook. *Smithells metals reference book*. Elsevier, 2013.

[8] Rodrigo Cassineli Palharini and Thomas Scanlon. *Atmospheric reentry modelling using an open source DSMC code*. PhD thesis, University of Strathclyde, 2014.

[9] Carlo Cercignani. *Rarefied gas dynamics: from basic concepts to actual calculations*, volume 21. Cambridge University Press, 2000.

[10] Carlo Cercignani and Adelia Daneri. Flow of a rarefied gas between two parallel plates. *Journal of Applied Physics*, 34(12):3509–3513, 1963.

[11] Dean R Chapman. Some possibilities of using gas mixtures other than air in aerodynamic research. pages 179–200, 1956.

[12] CFD Direct. Openfoam v6 user guide: 7.1 thermophysical models, 2018. URL https://cfd.direct/openfoam/user-guide/v6-thermophysical/.

[13] Jing Fan, Iain D Boyd, and Chris Shelton. Monte carlo modeling of electron beam physical vapor deposition of yttrium. *Journal of Vacuum Science & Technology A: Vacuum, Surfaces, and Films*, 18(6):2937–2945, 2000.

[14] Michele Giordano, Pietro Marco Congedo, and P Cinnella. Nozzle shape optimization for wet-steam flows. In *19th AIAA Computational Fluid Dynamic Conference*, 2009.

[15] OF Hagena and W Obert. Cluster formation in expanding supersonic jets: Effect of pressure, temperature, nozzle size, and test gas. *The Journal of Chemical Physics*, 56(5):1793–1802, 1972.

[16] Otto F Hagena. Nucleation and growth of clusters in expanding nozzle flows. *Surface Science*, 106(1-3):101–116, 1981.

[17] Otto F Hagena. Condensation in free jets: Comparison of rare gases and metals. *Zeitschrift für Physik D Atoms, Molecules and Clusters*, 4(3):291–299, 1987.

[18] Nancy Hall. Mass flow choking, 2018. URL https://www.grc.nasa.gov/www/k-12/airplane/mflchk.html.

[19] Francis H Harlow and Anthony A Amsden. Numerical calculation of almost incompressible flow. *Journal of Computational Physics*, 3(1):80–93, 1968.

[20] Hrvoje Jasak. Error analysis and estimation for the finite volume method with applications to fluid flows. 1996.

[21] Hrvoje Jasak. Dynamic mesh handling in openfoam. In *47th AIAA Aerospace Sciences Meeting Including the New Horizons Forum and Aerospace Exposition*, page 341, 2009.

[22] Hrvoje Jasak and Zeljko Tukovic. Automatic mesh motion for the unstructured finite volume method. *Transactions of FAMENA*, 30(2):1–20, 2006.

[23] James EA John. Gas dynamics. 1984.

[24] Mattias Karlsson, Ivo Alxneit, Frederik Rütten, Daniel Wuillemin, and Hans Rudolf Tschudi. A compact setup to study homogeneous nucleation and condensation. *Review of scientific instruments*, 78(3):034102, 2007.

[25] Saeed Jamali Keisari and Mehrzad Shams. Shape optimization of nucleating wet-steam flow nozzle. *Applied Thermal Engineering*, 103:812–820, 2016.

[26] PK Kundu, IM Cohen, G Hu, and DR Dowling. Fluid mechanics 6th ed., waltham, ma, 2015.

[27] LibreTexts. 10.9: Real gases - deviations from ideal behavior, 2003. URL https://chem.libretexts.org/Bookshelves/General_Chemistry/Map%3A_Chemistry_-_The_Central_Science_(Brown_et_al.)/10%3A_Gases/10.9%3A_Real_Gases_-_Deviations_from_Ideal_Behavior#title.

[28] William Louisos and Darren Hitt. Heat transfer & viscous effects in 2d & 3d supersonic micro-nozzle flows. In *37th AIAA Fluid Dynamics Conference and Exhibit*, page 3987, 2007.

[29] Shingo Matsuyama. Performance of all-speed ausm-family schemes for dns of low mach number turbulent channel flow. *Computers & Fluids*, 91:130–143, 2014.

[30] MIT. Basics of turbulent flow. URL http://www.mit.edu/course/1/1.061/www/dream/SEVEN/SEVENTHEORY.PDF.

[31] F Moukalled, L Mangani, M Darwish, et al. The finite volume method in computational fluid dynamics. *An advanced introduction with OpenFoam® and Matlab®. Nueva York: Springer. Recuperado de http://www. gidropraktikum. narod. ru/Moukalled-et-al-FVM-OpenFOAM-Matlab. pdf*, 2016.

[32] AK Rebrov. Free jets in vacuum technologies. *Journal of Vacuum Science & Technology A: Vacuum, Surfaces, and Films*, 19(4):1679–1687, 2001.

[33] RJ Riddell Jr and GE Uhlenbeck. On the theory of the virial development of the equation of state of monoatomic gases. *The Journal of Chemical Physics*, 21(11): 2056–2064, 1953.

[34] NW Ryan and MM Johnson. Transistion from laminar to turbulent flow in pipes. *AIChE Journal*, 5(4):433–435, 1959.

[35] Jung-Hee Seo and Young J Moon. Perturbed compressible equations for aeroacoustic noise prediction at low mach numbers. *AIAA journal*, 43(8):1716–1724, 2005.

[36] Felix Sharipov. Rarefied gas flow through a long rectangular channel. *Journal of Vacuum Science & Technology A: Vacuum, Surfaces, and Films*, 17(5):3062–3066, 1999.

[37] Felix Sharipov and Vladimir Seleznev. Data on internal rarefied gas flows. *Journal of Physical and Chemical Reference Data*, 27(3):657–706, 1998.

[38] Sule Yildiz Sirin. Effect of hot dip galvanizing on the fatigue behavior of hot rolled and ion nitrided aisi 4340 steel. *International Journal of Fatigue*, 123:1–9, 2019.

[39] Tata Steel. Automotive - metallic coated - serica, 2019. URL https://www.tatasteeleurope.com/en/products/automotive/metallic-coated/serica.

[40] Min Sun and Zhengyuan Ma. Effects of heat-treatment and hot-dip galvanizing on mechanical properties of rhs. *Journal of Constructional Steel Research*, 153: 603–617, 2019.

[41] George Wm Thomson. The antoine equation for vapor-pressure data. *Chemical reviews*, 38(1):1–39, 1946.

[42] HR Tschudi, M Karlsson, and DP Brown. Modelling of a steady nucleating flow in a laval nozzle. 2005.

[43] Tessa Uroić, Hrvoje Jasak, and Henrik Rusche. Implicitly coupled pressure–velocity solver. In *OpenFOAM®*, pages 249–267. Springer, 2019.

[44] Henk Kaarle Versteeg and Weeratunge Malalasekera. *An introduction to computational fluid dynamics: the finite volume method*. Pearson education, 2007.

[45] Elin Vesper. Large eddy simulation of heat transfer processes in energy systems based on thermodynamically consistent models. 2017.